A novel SUN1-ALLAN complex coordinates segregation of the bipartite MTOC across the nuclear envelope during rapid closed mitosis in Plasmodium

Mohammad Zeeshan[1+], Igor Blatov[1+], Ryuji Yanase[1#], David J. P. Ferguson[2#], Sarah L. Pashley[1], Zeinab Chahine[3], Yoshiki Yamaryo Botté[4], Akancha Mishra[1], Baptiste Marché[3], Suhani Bhanvadia[3], Molly Hair[2], Sagar Batra[1], Robert Markus[1], Declan Brady[1], Andrew Bottrill[5], Sue Vaughan[2], Cyrille Y. Botté[4], Karine Le Roch[3], Tony Holder[6], Eelco Tromer[7], Rita Tewari[1*]

[1]University of Nottingham, School of Life Sciences, Nottingham, UK.
[2]Oxford Brookes University, Department of Biological and Medical Sciences, Oxford, UK
[3]Department of Molecular, Cell and Systems Biology, University of California Riverside, 900 University Ave., Riverside, USA.
[4]Apicolipid Team, Institute for Advanced Biosciences, CNRS UMR5309, Université Grenoble Alpes, INSERM U1209, Grenoble, France
[5]School of Life Sciences, Gibbet Hill Campus, University of Warwick, Coventry, UK
[6]Malaria Parasitology Laboratory, The Francis Crick Institute, London, UK
[7]Cell Biochemistry, Groningen Biomolecular Sciences and Biotechnology Institute, Faculty of Science and Engineering, University of Groningen, Groningen, The Netherlands

* Rita.Tewari@nottingham.ac.uk
[+ #] These authors contributed equally

Short title: *Plasmodium* SUN1 and Allantoicase in BB/MTOC organisation

Abstract

Mitosis in eukaryotes involves reorganization of the nuclear envelope (NE) and microtubule-organizing centres (MTOCs). In *Plasmodium*, the causative agent of malaria, male gametogenesis mitosis is exceptionally rapid and divergent. Within 8 minutes, the haploid male gametocyte genome undergoes three replication cycles (1N to 8N), while maintaining an intact NE. Axonemes assemble in the cytoplasm and connect to a bipartite MTOC-containing nuclear pole and cytoplasmic basal body, producing eight flagellated gametes. The mechanisms coordinating NE remodelling, MTOC dynamics, and flagellum assembly remain poorly understood.

Here, we identify the SUN1-ALLAN complex as a novel mediator of NE remodelling and bipartite MTOC coordination during *Plasmodium* male gametogenesis. SUN1, a conserved NE protein, localizes to dynamic loops and focal points near nuclear spindle poles. ALLAN, a divergent Allantoicase-like protein, has a location like that of SUN1 at nuclear MTOCs. SUN1 and ALLAN form a unique complex, detected by live-cell imaging, ultrastructural expansion microscopy, and interactomics. Deletion of either SUN1 or ALLAN gene disrupts nuclear MTOC organization, leading to basal body mis-segregation, defective spindle assembly, and impaired kinetochore attachment, but axoneme formation remains intact. Ultrastructural analysis revealed nuclear and cytoplasmic MTOC miscoordination, producing aberrant flagellated gametes lacking nuclear material. Sun1 deletion also alters parasite lipid composition, underscoring its role in NE homeostasis. These defects block parasite development in the mosquito and transmission, highlighting the essential functions of this complex.

This study reveals a bipartite MTOC and a highly divergent mechanism of NE remodelling during *Plasmodium* male gametogenesis. The SUN1-ALLAN complex is an unusual adaptation of the LINC complex, in absence of canonical KASH-domain proteins in *Plasmodium*, providing new insights into the evolution of closed mitosis and highlighting potential targets for blocking malaria transmission.

Introduction

Mitosis, the process of eukaryotic cell division, requires the accurate segregation of nuclear and cytoplasmic materials, coordinated by dynamic changes in the nuclear envelope (NE) and microtubule-organizing centres (MTOCs) (Liu and Pellman, 2020). The NE, a double-membrane structure with embedded nuclear pore complexes, is a selective barrier, facilitating signal exchange between cytoplasm and nucleus. Beyond these structural and transport roles, the NE is integral to mitosis, supporting spindle formation, kinetochore attachment, and chromosome segregation, while also accommodating changes in ploidy (Dey and Baum, 2021; Smoyer and Jaspersen, 2014).

There are two primary modes of NE remodelling during mitosis. In most mammalian cells, mitosis is ‘open’, characterized by complete NE disassembly, and chromosome condensation and segregation via a microtubule-based bipolar spindle. In contrast, in unicellular organisms such as the budding yeast *Saccharomyces cerevisiae,* mitosis is ‘closed’: the NE remains intact, and chromosomes are segregated by an intranuclear spindle anchored to acentriolar nuclear poles (Boettcher and Barral, 2013; Sazer et al., 2014). The NE consists of inner (INM) and outer (ONM) membranes, with the ONM continuous with the endoplasmic reticulum (ER). Closed mitosis involves diverse NE dynamics: for example, *Trypanosoma* and *Saccharomyces* employ intranuclear spindle assembly, whereas *Chlamydomonas* and *Giardia* assemble spindles outside the nucleus, the NE remains largely unbroken, but large polar fenestrae are formed to allow microtubule access to the chromosomes (Makarova and Oliferenko, 2016). These examples highlight the evolutionary diversity of NE remodelling.

The interaction between nucleus and cytoskeleton is facilitated by the LINC (Linker of Nucleoskeleton and Cytoskeleton) complex, a structure present in most eukaryotes. LINC bridges the INM and ONM via interactions between SUN (Sad1, UNC84)-domain proteins on the INM and KASH (Klarsicht, ANC-1, Syne Homology)-domain proteins on the ONM (Hao and Starr, 2019; Starr and Fridolfsson, 2010). Evolutionary studies suggest that LINC was established before the emergence of the last eukaryotic common ancestor (LECA), highlighting its ancient role in NE

formation and cytoskeletal coordination (Baum and Baum, 2014; Koreny and Field, 2016).

The malaria-causing parasite *Plasmodium spp.* uses closed mitosis with some highly divergent features across its complex life cycle. In the asexual stage in the blood of its vertebrate host, during schizogony there is asynchronous nuclear division without coincident cytokinesis, and during male gametogenesis in the mosquito host there is a unique and rapid form of closed mitosis essential for parasite transmission (Guttery et al., 2022; Sinden et al., 1978). Following activation in the mosquito gut, the haploid male gametocyte undergoes three rounds of genome replication (from 1N to 8N) within just 6 to 8 minutes, while maintaining an intact NE. Concurrently, axonemes form in the cytoplasm, emanating from bipartite MTOCs that consist of intranuclear spindle poles and cytoplasmic basal bodies (BB). This rapid karyokinesis and subsequent cytokinesis results in the production of eight flagellated haploid male gametes within 15 minutes (Guttery et al., 2022).

The rapidity of male gametogenesis in *Plasmodium* imposes unique requirements and constraints on cellular structures. Notably, the flagella lack intraflagellar transport (IFT), which is atypical (Sinden et al., 2010). A bipartite organization of the MTOC, comprising nuclear spindle pole and cytoplasmic BB, was recently revealed, and use of fluorescently tagged markers such as SAS4 and kinesin-8B has illuminated the dynamics of BB and axoneme formation (Zeeshan et al., 2022a; Zeeshan et al., 2019a). Kinetochore proteins like NDC80 display an unconventional, largely clustered linear organization on the spindle, redistributing only during successive spindle duplication (Zeeshan et al., 2020). Remarkably, successive spindle and BB segregation occurs within 8 minutes of gametocyte activation, without NE breakdown, indicating an unusual, streamlined closed mitotic process (Zeeshan et al., 2022a; Zeeshan et al., 2019a).

Despite the remarkable speed and complexity of closed mitosis in *Plasmodium* male gametogenesis, the mechanisms that coordinate the formation and function of the intranuclear spindle poles, the cytoplasmic BB, and the NE remain unclear. Specifically, how the NE is remodelled to accommodate rapid genome replication, and organization of the bipartite MTOC remain open questions. We addressed these questions by investigating NE remodelling and MTOC coordination in *Plasmodium berghei* (Pb), using the conserved NE protein SUN1, a key component of the link

between the nuclear interior and the cytoplasmic cytoskeleton in many eukaryotes. By combining live-cell imaging, ultrastructural expansion microscopy (U-ExM), and proteomic analysis, we identify SUN1 as a key NE component. Using different mitotic and MTOC/BB markers, we show the coordination and flexibility of NE during rapid mitosis. Our findings reveal that SUN1 interacts with a novel Allantoicase-like protein (termed ALLAN), to form a divergent LINC-like complex without KASH proteins. Functional disruption of either SUN1 or ALLAN impairs BB segregation, disrupts kinetochore attachment, and results in defective flagellum assembly. SUN1 elimination also alters lipid homeostasis, suggesting a broader role in NE organization and metabolic regulation. Our results highlight the unique divergence from classical eukaryotic models (e.g. fungi and animals), of NE remodelling and MTOC organization in *Plasmodium* gametogenesis.

Results

Generation and Validation of PbSUN1 Transgenic Lines

To investigate the role of PbSUN1 (PBANKA_1430900) during *Plasmodium berghei* male gametogenesis, we generated transgenic parasite lines expressing either a C-terminal GFP-tagged (SUN1-GFP) or mCherry-tagged (SUN1-mCherry) SUN1 protein. The GFP-tagging construct was integrated into the 3′ end of the endogenous *sun1* locus via single-crossover recombination **(Fig. S1A)**, and correct integration was confirmed by PCR analysis using diagnostic primers **(Fig. S1B)**. Western blot analysis detected SUN1-GFP at the expected size (~130 kDa) in gametocyte lysates **(Fig. S1C)**. Similar validation confirmed successful generation of the SUN1-mCherry line **(Fig. S1D)**. Both tagged lines showed normal parasite growth and progression through the life cycle, indicating that tagging did not disrupt PbSUN1 function. These transgenic lines were used to study the subcellular localization of PbSUN1 across multiple life cycle stages, and its interaction with other proteins during gametogenesis.

Spatiotemporal dynamic of SUN1 During Male Gametogenesis

Live-cell imaging detected no SUN1 protein expression during asexual erythrocytic stages of the parasite, but robust expression in both male and female gametocytes following activation in ookinete medium (**Fig. S1E, S1F**). In activated male gametocytes undergoing mitotic division, SUN1-GFP displayed a dynamic localization around the nuclear DNA (Hoechst-stained), associated with loops and folds forming in the nuclear envelope (NE) during the transition from 1N to 8N ploidy (**Fig. 1A**). The NE loops extended beyond the Hoechst-stained DNA, suggesting abundant membrane and a non-spherical shape for the NE (**Fig. 1A**). To further characterize the NE morphology during male gametogenesis, serial block-face scanning electron microscopy (SBF-SEM) was used. Analysis of wild-type male gametocytes revealed a non-spherical, contorted nucleus (**Fig. 1B, S1G**). Thin loops of NE (arrows) were prominent, consistent with the dynamic and irregular localization of SUN1-GFP observed by live-cell imaging. 3D-modelling of gametocyte nuclei further confirmed this irregular, non-spherical NE structure (**Fig. 1C, S1H**), which expands rapidly during the eightfold genome replication. These findings suggest that the male gametocyte NE is a highly dynamic structure that can expand rapidly to accommodate the DNA replication during gametogenesis.

SUN1 dynamics by High-Resolution Imaging

To refine the spatial relationship of SUN1 to the BB and spindle, ultrastructure expansion microscopy (U-ExM) was employed. At 5 to 6 minutes post-activation, SUN1-GFP was prominently located around the DNA and at the junction of the nuclear MTOC and the BB (**Fig. 1D**). Spindle and axoneme staining with α-tubulin antibodies revealed that SUN1-GFP was enriched near spindle poles (**Fig. 1E**), suggesting a role in NE organization during mitosis. To resolve the SUN1-GFP location with higher precision, structured illumination microscopy (SIM) was performed on fixed SUN1-GFP gametocytes. However, an uneven SUN1-GFP signal intensity around DNA (**Fig S1I**) was observed, with areas of higher intensity (white arrows) likely representing collapsed forms of the loops observed by live imaging. It appears that fixation with paraformaldehyde caused collapse of the NE loops and folds associated with SUN1-GFP, disrupting the dynamic structure.

SUN1 Localization Relative to Key Mitotic Markers During Male Gametogenesis

To investigate the association of SUN1 with MTOCs, mitotic spindles, and BB/axonemes during male gametogenesis, its location in real time was compared with that of three markers: the cytoplasmic BB/axonemal protein kinesin-8B, the spindle microtubule-binding protein EB1, and the kinetochore marker NDC80 (Zeeshan et al., 2019; 2020; 2023). A parasite line expressing SUN1-GFP (green) was crossed with lines expressing mCherry (red)-tagged kinesin-8B, EB1, or NDC80, and progeny were analyzed by live-cell imaging to determine their spatiotemporal relationships.

Within one-minute post-activation, kinesin-8B appeared as a tetrad marking the BB in the cytoplasm and close to the nucleus, while SUN1-GFP localized to the nuclear membrane with no overlap (**Fig. 1F**). As gametogenesis progressed, nuclear elongation was observed, with SUN1-GFP delineating the nuclear boundary. Concurrently, the BB (the kinesin-8B-marked tetrad) duplicated and separated to opposite poles in the cytoplasm, outside the SUN1-GFP-defined nuclear boundary (**Fig. 1F**). By 2 to 3 minutes post-activation, axoneme formation commenced at the BB (kinesin-8B-positive), while SUN1-GFP marked the NE with strong signals located near the nuclear MTOCs situated between the BB tetrads (**Fig. 1F**).

Analysis of SUN1-GFP and the spindle microtubule marker EB1 revealed a localized EB1-mCherry signal near the DNA, inside the nuclear membrane (marked by SUN1-GFP), within the first minute post-activation (**Fig. 1G**). Loops and folds in the nuclear membrane, marked by SUN1-GFP, partially overlapped with the EB1 focal point, which is associated with the spindle pole/MTOC (**Fig. 1G**). At 2 to 3 min post activation, EB1 extended to form a bridge-like spindle structure within the nucleus, flanked by two strong focal points that partially overlapped with SUN1-GFP fluorescence (**Fig. 1G**). A similar dynamic location was observed for another spindle protein, ARK2 **(Fig. S2A).**

Kinetochore marker NDC80 showed a similar pattern to that of EB1. Within one-minute post-activation, NDC80 was detected as a focal point inside the nuclear membrane, later extending to form a bridge-like structure that split into two halves within 2 to 3 minutes, and with no overlap with SUN1-GFP (**Fig. 1H**). As with EB1, the nuclear membrane loops formed around NDC80 focal points, maintaining close proximity to the kinetochore bridge (**Fig. 1H**).

Together, these observations suggest that although SUN1-GFP is partially colocalized with spindle poles as indicated by EB1, it shows no overlap with kinetochores (NDC80) or BB/axonemes (kinesin-8B).

SUN1 Location During Female Gametogenesis and Zygote to Ookinete transformation

The location of SUN1-GFP during female gametogenesis was examined using real-time live-cell imaging. Within one-minute post-activation, SUN1-GFP was observed to form a half-circle around the nucleus, eventually encompassing the entire nucleus by six to eight minutes (**Fig. S2B**). In contrast to SUN1-GFP in male gametocytes, SUN1-GFP in female gametocytes was more uniformly distributed around the nucleus without apparent loops or folds in the NE (**Fig. S2B**). This pattern probably reflects the absence of DNA replication and mitosis in female gametogenesis, so that the nucleus remains compact.

During zygote to ookinete differentiation and oocyst development, in zygotes, SUN1-GFP had a spherical distribution around Hoechst-stained nuclear DNA at two hours post-fertilization (**Fig. S2C**), but by 24 hours post-fertilization, as the zygote developed into a banana-shaped ookinete, the SUN1-GFP-marked NE became

elongated or oval, possibly due to spatial constraints within the cytoplasm (**Fig. S2C)**.

SUN1 Is Essential for Basal Body Segregation and Axoneme-Nucleus Coordination During Male Gametogenesis

The role of SUN1 was assessed by deleting its gene using a double crossover homologous recombination strategy in a parasite line constitutively expressing GFP (WT-GFP) (Janse et al., 2006) (**Fig. S3A**). WT-GFP parasites express GFP at all stages of the life cycle, facilitating phenotypic comparisons. Diagnostic PCR confirmed the correct integration of the targeting construct at the *sun1* locus (**Fig. S3B**), and this was verified by qRT-PCR analysis, which showed complete deletion of the *sun1* gene in the resulting transgenic parasite (*Δsun1*) (**Fig. S3C**).

Phenotypic analysis of the *Δsun1* line was conducted across the life cycle, in comparison to a WT-GFP control. Two independent knockout clones (Clone-1 and Clone-4) were examined: the clones exhibited similar phenotypes, and one, Clone-4 was used for further experiments. *Δsun1* parasites produced a comparable number of gametocytes to WT-GFP parasites, but had reduced male gametogenesis, as evidenced by a significant decrease in gamete formation (exflagellation) (**Fig. 2A**). The differentiation of zygotes into ookinetes was also reduced (**Fig. 2B**).

To evaluate sporogonic development, mosquitoes were fed with *Δsun1* parasites, and oocyst formation was examined. The number of oocysts was markedly reduced in *Δsun1* parasite-infected mosquitoes compared to WT-GFP parasites at days 7, 14, and 21 post-feeding (**Fig. 2C**). At day 7, oocysts were comparable in size but failed to grow further, and they had degenerated by day 21 (**Fig. 2D**). Transmission experiments revealed that mosquitoes infected with *Δsun1* parasites were unable to transmit the parasite to naïve mice; in contrast mosquitoes successfully transmitted the WT-GFP parasite, resulting in a blood-stage infection detected four days later (**Fig. S2D**).

Because the defect in *Δsun1* parasites led to a transmission block, we investigated whether the defect was rescued by restoring *sun1* into *Δsun1* parasites, using the *Δnek4* parasite that produces normal male gametocytes but is deficient in production of female gametocytes. We performed a genetic cross of *Δsun1* and *Δnek4* parasites, which produced some normal-sized oocysts that were able to sporulate, showing a partial rescue of the *Δsun1* phenotype **(Fig. 2E).** As controls,

Δsun1 and *Δnek4* parasites alone were examined and no oocysts/sporozoites were detected **(Fig. 2E).** These results indicate that a functional *sun1* gene is required from a male gamete for subsequent oocyst development.

Transcriptomic analysis of *Δsun1* gametocytes shows modulation in lipid metabolism and microtubule organization

To investigate the effect of *sun1* deletion on transcription, we performed RNA-seq analysis in triplicate on *Δsun1* and in duplicate on WT-GFP gametocytes, at 8 min and 30 min post-activation. Total RNA was extracted at these two time points to detect early and late changes in gene expression post-activation. Pairwise correlation analyses of *Δsun1* and WT-GFP gametocytes at the two time points confirmed the reproducibility of these RNA-seq experiments. A detailed analysis of the mapped reads also confirmed the deletion of *sun1* in the *Δsun1* strain (**Fig. S3E, F**). A relatively small number of differentially expressed genes was identified in both 8 min and 30 min samples, with 115 and 82 genes, respectively (**Fig. 2F, G**; Supplementary **Table S1**). Of the perturbed genes, 42 and 31 were significantly downregulated, and 73 and 51 were significantly upregulated in *Δsun1* parasites relative to WT-GFP controls at 8 min and 30 min, respectively (**Fig. 2F, G**; **Supplementary Table S1**). Gene ontology (GO)-based enrichment analysis of these genes showed that several genes upregulated at both 8 min and 30 min were involved in either lipid metabolic processes, microtubule cytoskeleton organization, or microtubule-based movement (**Fig. 2H, I**). These findings suggest that lipid metabolism and microtubule function may be critical functions for gametogenesis that can be perturbed by *sun1* deletion.

Disruption of SUN1 Perturbs Lipid Homeostasis and Membrane Biogenesis in Gametocytes

Given the nuclear membrane location of SUN1 and the upregulated expression of genes involved in lipid metabolism in *Δsun1* gametocytes, we investigated the lipid profile of *Δsun1* and WT-GFP gametocytes using mass spectrometry-based lipidomic analyses (**Fig. 2J).** Lipids are key elements of membrane biogenesis, with most phospholipids derived from fatty acid precursors. Lipids also play roles in signal transduction, storage (e.g., neutral lipids such as triacylglycerol [TAG] and

cholesteryl esters [CE]), and modulation of membrane curvature (Amiar et al., 2020; Shunmugam et al., 2022).

We compared the lipid profile of *Δsun1* and WT-GFP gametocytes, either non-activated (0 min) or activated (8 min). Both the disruption of SUN1 and the activation of gametocytes caused significant changes in the amounts of phosphatidic acid (PA), CE, monoacylglycerol (MAG), and TAG. Activated gametocytes had increased levels of PA, TAG, and CE and a decreased level of free fatty acids (FFA), compared to non-activated gametocytes (**Fig. 2K, L**).

Interestingly, *Δsun1* gametocytes had significantly lower PA and CE levels prior to activation and a less pronounced increase in these lipids upon activation. Conversely, MAG and diacylglycerol (DAG) levels were higher in *Δsun1* gametocytes at both 0 min and 8 min compared to WT-GFP (**Fig. 2K, L**). There was also a differential response to activation in lysophosphatidylcholine (LPC) and specific fatty acid compositions **(Fig S3G)**. Notably, the *Δsun1* mutant had altered levels of arachidonic acid (C20:4), a scavenged fatty acid precursor of inflammatory molecules such as leukotrienes and prostaglandins **(Fig S3H)** (Botte et al., 2013; Dubois et al., 2018), and an increase in myristic acid (C14:0), a product of apicoplast fatty acid synthesis (FASII) **(Fig S3H)** (Amiar et al., 2020; Botte et al., 2013). The altered lipid profiles suggest that *sun1* deletion causes a disruption in lipid homeostasis and that SUN1 plays a crucial role, linking lipid metabolism to NE remodelling and gamete formation.

Ultrastructural microscopy reveals defects in spindle formation, Basal Body segregation and nuclear attachment to axonemes in *Δsun1* gametocytes

To define the ultrastructural defects caused by *sun1* deletion, we used ultrastructure expansion microscopy (U-ExM) and transmission electron microscopy (TEM) to examine the morphology of male gametocytes at critical time points - 1.5-, 8-, and 15-min post-activation, representing the timing of major transitions in spindle formation, BB segregation, and axoneme elongation (**Fig. 3A-D, Fig. S4, 5**).

U-ExM revealed that in WT-GFP gametocytes, spindle microtubules were robustly assembled by 1.5 min post-activation, extending from nuclear MTOCs (spindle poles) to kinetochores. Simultaneously, BB - marked by NHS ester staining - segregated into tetrads, distributed across the cytoplasmic periphery (**Fig. 3A, S4A**). By 8 min, spindles were fully extended, ensuring accurate chromosome segregation,

while BB had replicated to nucleate parallel axonemes aligned around the nucleus (**Fig. S4B**). By 15 min, these processes had culminated in exflagellation, producing mature microgametes containing nuclei tightly associated with BB-derived axonemes (**Fig. 3B, S4C**). In Δ*sun1* gametocytes, these processes were severely disrupted. At 1.5 min, α-tubulin staining showed incomplete or malformed spindles. NHS ester staining revealed BB clumped near one side of the nucleus, indicating a failure in segregation (**Fig. 3A, S4A**). By 8 min, spindles remained rudimentary, and BB segregation was still incomplete. Axoneme elongation proceeded, but BB and nuclear poles failed to align, leading to misconnected or unconnected axonemes (**Fig. S4B**). At 15 min, gametes emerged from cytoplasmic protrusions, but many lacked nuclei due to the absence of proper BB segregation and nuclear compartmentalization (**Fig. 3B)**.

We performed TEM analysis of *Δsun1* and WT-GFP gametocytes at 8- and 15 min post-activation. At 8 min post-activation, many of the wildtype male gametocytes had progressed to the third genome division with multiple nuclear spindle poles within a central nucleus **(Fig 3Da).** In many cases, a BB was visible, closely associated with and connected to the nuclear pole **(Fig 3Db, c).** From the nuclear pole, nuclear spindle microtubules (SMt) radiated into the nucleoplasm and connected to kinetochores **(Fig 3Db, c).** Within the cytoplasm several elongated axonemes, some with the classical 9+2 microtubule arrangement, were visible **(Fig 3Da, c).**

At 8 min in *Δsun1* gametocytes there were predominately mid stage forms with elongated axonemes running around the nucleus **(Fig 3Dd; S5Aa).** It was also possible to find clumps (groups) of BB **(Fig 3Dd, e; S5 Aa, b).** However, there was little evidence of BB association with nuclear poles **(Fig 3De).** It was also difficult to find nuclear spindle microtubules**,** but free kinetochores were often observed in the nucleoplasm **(Fig 3Df, S5 Ac)**. Nevertheless, the parallel orientation of the axonemes appeared to be maintained and many displayed the normal 9+2 arrangement **(Fig 3Dc).**

By 15 min, WT-GFP gametocytes showed exflagellation, displaying BB at the tip of the flagellum. Cross sections showed gametes with normal axonemes with a 9+2 arrangement and an enclosed nucleus surrounded by a plasma membrane **(Fig 3Dg, h).** In *Δsun1* samples, several late stages as well as some mid stages were observed. The late stages had more electron dense cytoplasm **(Fig 3Di).** The

majority had few if any axonemes, but all had a large nucleus with small clumps of electron dense material **(Fig 3Di).** A few male gametocytes appeared to be undergoing exflagellation with flagellar-like structures protruding from the cell surface, often with multiple axonemes **(Fig 3Di, j)**. However, they were abnormal, lacking a nucleus and often with variable numbers (1 to 6) of normal 9+2 axonemes **(Fig 3Dj, k, l)**. There appeared to be a disconnect between the axonemes and nucleus (nuclear poles) during exflagellation with no condensation of the nuclear chromatin to form individual microgamete nuclei. This *Δsun1* mutant appeared to have a problem forming nuclear spindles and dividing its genome. The nuclear spindle poles were difficult to find and do not appear to be able to divide or move apart. It is possible that this lack of spindle pole division and movement was responsible for the BB remaining clumped together in the cytoplasm. It is also possible that clumping of the BB may explain the presence of multiple axonemes associated with the exflagellated structures. Additional examples of *Δsun1* phenotype at 15 min are shown in **Fig S5B**. The quantification data for the *Δsun1* phenotypes are shown in **Fig 3D-G** and **Fig S5C.**

Together, these findings highlight the pivotal role of SUN1 in coordinating the nuclear and cytoplasmic compartments during male gametogenesis. Its absence disrupts spindle formation, BB segregation, and the physical attachment of axonemes to the nucleus, resulting in anuclear flagella and defective gametes incapable of fertilization.

SUN1 Interactome Reveals Associations with Nuclear Envelope, ER and Chromatin components

To identify protein interaction partners of PbSUN1, we performed GFP-based immunoprecipitation (IP) using a nanobody targeting SUN1-GFP in lysates of purified gametocytes activated for 6 to 8 min. This time point was chosen as it coincides with peak nuclear expansion and axoneme formation. To stabilize transient or weak interactions, protein cross-linking with 1% paraformaldehyde was used prior to IP. Co-immunoprecipitated proteins were identified using LC-MS/MS of tryptic peptides and were analysed using principal component analysis for duplicate WT-GFP and SUN1-GFP precipitations. (**Fig. 4A, Supplementary Table S2**).

Co-variation with SUN1 was found for proteins of the nuclear envelope, chromatin and ER-related membranes. Notably, SUN1 co-purified with nuclear pore

proteins (NUP269, NUP335), membrane proteins, including a likely ER component (DDRGK-domain containing UFM1 E3 ligase, PBANKA_0927700), chromatin-related factors (e.g. condensin I/II subunits, topoisomerase II), and the cytoplasmic and male gametocyte-specific kinesin-15 (PBANKA_145880). This suggests a role for SUN1 in bridging chromatin (through condensin II) on the nuclear side and the cytoskeleton (through kinesin-15) on the cytoplasmic side of the nuclear envelope, potentially in association with nuclear pores (**Fig. 4A**) in a similar fashion to what has been proposed in the plant Arabidopsis (Ito et al., 2024; Sakamoto et al., 2022).

PbSUN1 also interacted with proteins harbouring a divergent carbohydrate-binding domain (like SUN1 itself), such as the allantoicase-like protein ALCC1 (Sayers et al. 2024), here referred to as ALLAN (PBANKA_1144200) and PBANKA_0209200, an ER-Golgi protein with a mannose-binding domain (**Fig. 4A, Supplementary Table S2**). ALLAN is an uncharacterized protein with sequence homology to allantoicase, an enzyme of purine metabolism. We could detect no KASH-like or lamin-like proteins co-immunoprecipitated with SUN1; these are the hallmark ONM/INM partners of SUN-domain proteins in classical LINC complexes, respectively. To further explore the interaction between ALLAN and SUN1, we immunoprecipitated ALLAN-GFP, from lysates of gametocytes 6-min post activation. Amongst the interactors we found SUN1 and its interactors, DDRGK-domain containing protein and kinesin-15 (**Fig. 4B, Supplementary Table S2**). The results from the immunoprecipitation experiments suggest that *Plasmodium* SUN1 functions in a non-canonical fashion via an interaction with ALLAN to tether chromatin to the nuclear envelope and ultimately to the cytoplasmic cytoskeleton via kinesin-15 (**Fig. 4D**).

We hypothesized that SUN1 is at the centre of multiple molecular interactions during male gametogenesis, coordinating NE remodelling, spindle organization, and BB/axoneme attachment, with ALLAN as a key interactor near the nuclear MTOC. Therefore, we studied the role of ALLAN.

ALLAN is located at nuclear poles (NP) and influences Basal Body/NP segregation in male gametogenesis

To reveal ALLAN's function in the *Plasmodium* life cycle, we generated a C-terminal GFP-tagged ALLAN parasite line, confirming correct integration by PCR (**Fig. S6A, B**) and detecting a protein of ~85 kDa by Western blot (**Fig. S6C**). ALLAN-GFP

parasites displayed normal growth and completed the life cycle, indicating that GFP tagging did not impair protein function.

During asexual blood stages, ALLAN-GFP exhibited a diffuse nucleoplasmic signal in trophozoites and schizonts with distinct focal points adjacent to dividing DNA, consistent with a role in mitotic regulation (**Fig. S6D**). However, by late schizogony, the ALLAN signal had diminished. In male and female gametocytes **(Fig S6E)** and during zygote to ookinete transformation **(Fig S6F),** ALLAN-GFP showed a spherical distribution around Hoechst-stained nuclear DNA and was enriched to form distinct focal points. During oocyst development and liver schizogony, ALLAN-GFP also exhibited distinct focal points adjacent to dividing DNA **(Fig S6G, H)** suggesting a role in mitotic regulation, like in asexual blood stages **(Fig. S6D).**

In activated male gametocytes, ALLAN-GFP rapidly localized within a minute post-activation to the NE, forming strong focal points that correlated with spindle poles or MTOCs (**Fig. 5A**). This localization persisted as ploidy increased from 1N to 8N in successive rounds of genome replication during male gametogenesis (**Fig. 5A**). Using U-ExM, ALLAN-GFP was resolved at the INM, enriched at spindle poles marked by NHS-ester staining, but absent from BB, where axonemes form during male gametogenesis (**Fig. 5B, 5C**). The location of ALLAN-GFP showed no overlap with that of kinesin-8B, a BB marker, and that of kinetochore marker NDC80 (**Fig. 5D, F**). Conversely, crosses with EB1-mCherry, a spindle marker, revealed an overlap at spindle poles (**Fig. 5E**) suggesting a role for ALLAN in nuclear spindle pole organization. Thus, the spatial relationship of SUN1 and ALLAN suggests coordinated roles in nuclear architecture and division of labour. SUN1 likely spans the NE, linking nuclear and cytoplasmic compartments, while ALLAN localizes more specifically to nuclear MTOCs.

The proximity of both SUN1 and ALLAN at spindle poles is consistent with their collaboration to align spindle microtubules with nuclear and cytoplasmic MTOCs and ensure that chromosomal segregation aligns with axoneme formation. We performed functional studies of ALLAN deletion mutants to examine its contribution to spindle dynamics and its potential as a key player in the rapid *Plasmodium* closed mitosis.

Functional Role of ALLAN in Male Gametogenesis

We generated *Δallan* mutants using double-crossover homologous recombination. Correct integration and successful gene deletion were confirmed via PCR (**Fig. S7A, S7B**) and qRT-PCR, with no residual allan transcription in *Δallan* lines (**Fig. S7C**). There was no phenotype in asexual blood stages, but *Δallan* mutants exhibited significant defects in mosquito stages.

Δallan parasites showed no marked reduction in male gamete exflagellation compared to WT-GFP controls (**Fig. 6A**), and ookinete conversion rates were slightly reduced (**Fig. 6B**). However, oocyst counts were significantly lower in *Δallan*-parasite infected mosquitoes, with diminished oocyst size and survival at 14- and 21-days post-infection (**Fig. 6C, D**). However, *Δallan* parasites were successfully transmitted to mice in bite-back experiments, showing that some viable sporozoites were produced (**Fig. 6E**).

U-ExM analysis revealed a striking defect in Δ*allan* male gametocyte morphology. At 8 min post-activation, NHS-ester staining indicated clustered BB, with incomplete segregation and misalignment relative to the nuclear MTOCs (**Fig. 6F**). Despite normal axoneme elongation, spindle organization was disrupted, as seen in nonsegregated BB/MTOCs (**Fig. 6F**).

To further explore the structural changes, we used electron microscopy analysis of gametocytes fixed at 8 min and 15 min post activation **(Fig 6G).** At 8 min in the WT parasite there was a lobated nucleus exhibiting nuclear poles showing nucleoplasm microtubules associated with kinetochores and with closely associated BB on the cytoplasmic side **(Fi 6Ga, b, c).** By 15 min free microgametes (flagella) were also observed showing 9+2 axonemes with nucleus **(Fig 6Gd, e).** In the *Δallan* mutant, numerous mid stage microgametocytes were observed. In the cytoplasm it was possible to find a few clumps of BB-like structures, although several were disorganised **(Fig 6Gf, g).** In a significant proportion of cells, the nucleus exhibited free kinetochores with no associated spindle microtubules **(Fig 6Gh)** and it was difficult to find nuclear poles or obvious nuclear spindles. A nuclear pole-like structure was often associated with the clump of electron dense material **(Fig 6Gg)**. Additional examples of *Δallan* phenotype are shown in **Fig S8A**.

By 15 min post-activation in *Δallan* gametocyte samples there were numerous free flagella - most with no nucleus **(Fig 6Gi)**. Some had multiple axonemes **(Fig 6Gj)** but there were many fewer examples than seen in the *Δsun1*. A few male gametes with axonemes and associated nuclei were observed. Additional examples

of *Δallan* phenotype are shown in **Fig S8B**, and the quantification of *Δallan* phenotype data is shown in **Fig 6H-J** and **Fig S8C.**

These *Δallan* defects suggest that ALLAN is critical for the alignment of spindle microtubules with kinetochores and BB segregation. The lack of spindle assembly and impaired nuclear pole organization in *Δallan* gametocytes is reminiscent of the *Δsun1* mutant phenotype, reinforcing the relationship between these two proteins.

Evolution of a novel SUN1-ALLAN axis in Haemosporida

The non-canonical SUN1-ALLAN complex in *P. berghei* is a unique apicomplexan adaptation, where NE and MTOC dynamics diverge from those of other eukaryotes. To trace the evolution of this interaction, we examined SUN1, ALLAN, and potential interactors (e.g., KASH proteins and lamins) across apicomplexans, dinoflagellates, ciliates, and model organisms such as yeast, humans, and *Arabidopsis* (**Fig. 7, Supplementary Table S3**).

SUN domain proteins generally fall into two families: C-terminal SUN domain and N-terminal/mid SUN domain proteins (Graumann et al., 2014). Most eukaryotes have representatives of both families. *P. berghei* has two SUN domain proteins (Kandelis-Shalev et al, 2024), one of each family with PbSUN1 having a C-terminal SUN domain. Allantoicase-like proteins often consist of two domains, belonging to the galactose-binding group that are remarkably similar to the SUN domain, (**Fig. 7A**). Among apicomplexans, two allantoicase subtypes are present due to duplication in the ancestor of all Apicomplexa: AKiT8 (Brusini et al., 2022) a kinetochore-associated protein, and ALLAN, the allantoicase-like subtype. Notably, *Plasmodium* is one of the few apicomplexans retaining both subtypes. Sequence divergence complicates phylogenetic classification of allantoicase-like proteins, but length-based classification distinguished the longer AKiT8 (~2300 aa) from ALLAN-like proteins (~800 aa; **Fig. 7B**). Despite using previously developed Hidden Markov Model and structural searches (Benz et al., 2024), we found no evidence of KASH-domain proteins or lamins in amongst apicomplexans, as in prior studies (**Fig. 7B**) (Koreny and Field, 2016).

AlphaFold3 (AF3) modelling revealed that SUN1 and ALLAN interact specifically in Haemosporida through the N-terminal domain of SUN1, a region that is absent from other apicomplexan and/or eukaryotic SUN1 family proteins (**Fig. 7C**).

We could not detect similar interactions between SUN1-like and ALLAN-like orthologs amongst other apicomplexans, ruling out a rapidly evolving interaction. Based on these structural predictions and the super-resolution imaging of SUN1- and ALLAN-GFP lines **(Fig. 1D, E; Fig. 5B, C**), we propose that ALLAN resides on the nucleoplasmic side of the NE, while SUN1's C-terminal domain likely extends toward the ONM to interact with proteins involved in axoneme and cytoskeletal dynamics in the nucleoplasm (**Fig. 7D**). This specificity may underscore the restricted nature of a SUN1-ALLAN complex to Haemosporida, and thus specific adaption of the allantoicase-like protein ALLAN for nuclear envelope dynamics..

Discussion

This study identifies the SUN1-ALLAN complex as a novel and essential mediator of NE remodelling and bipartite MTOC coordination during *P. berghei* male gametogenesis. *Plasmodium* lacks KASH-domain proteins and lamins, and a canonical LINC complex, relying on a highly divergent mechanism to tether nuclear and cytoplasmic compartments during rapid closed mitosis (Rout et al., 2017).

Our results reveal that SUN1 and ALLAN form a unique complex essential for spindle assembly, BB segregation, and axoneme organization, maintaining an intact NE throughout. Disruption of either protein causes spindle and MTOC miscoordination, leading to defective male gametes incapable of fertilization. Additionally, SUN1 deletion alters lipid homeostasis and NE dynamics, underscoring its multifaceted role in nuclear organization and metabolism. These findings establish the SUN1-ALLAN axis as a crucial evolutionary innovation in *Plasmodium* and as a promising target for blocking malaria transmission.

Mitosis is a fundamental process of eukaryotic cell division, requiring precise chromosome segregation, which is often coordinated through the NE (Liu and Pellman, 2020). In classical models of mitosis, such as in yeast and mammalian cells, there are distinct variations in NE remodelling. In open mitosis, as seen in mammals, the NE disassembles entirely, allowing cytoplasmic spindle assembly. In contrast, in closed mitosis, as observed in yeast, the NE remains intact, and spindle poles are embedded within the NE, forming intranuclear spindles (Dey and Baum, 2021; Sazer et al., 2014). These systems are further supported by the LINC complex, composed of SUN-domain proteins in the INM and KASH-domain proteins

in the ONM, to facilitate nuclear-cytoskeletal coordination. Altogether the LINC complex connects the intranuclear environment with NE proteins like lamins and the chromatin via for instance condensin-II with the extranuclear cytoskeleton (Tzur et al., 2006).

In *P. berghei* male gametogenesis, mitosis is closed and extraordinarily rapid with features that diverge significantly from those of classical models. Within just 8 min, there are three rounds of DNA replication (1N to 8N), accompanied by the assembly of axonemes on cytoplasmic BB (Guttery et al., 2022). KASH-domain proteins and lamins are absent, yet *Plasmodium* achieves precise nuclear and cytoskeletal coordination. Our findings reveal that this is accomplished through a non-canonical SUN1-ALLAN complex. SUN1 located at the NE, forms loops and folds to accommodate rapid nuclear expansion, and ALLAN facilitate spindle pole coordination.

Recent studies on SUN1-doamin containing proteins have been reported in some Apicomplexa parasites including *Toxoplasma* and *Plasmodium* (Kandelis-Shalev et al., 2024; Sayers et al., 2024; Wagner et al., 2023). SUN like protein-1 of Toxoplasma gondii shows a mitotic spindle location and is important for nuclear division (Wagner et al., 2023). *Plasmodium spp.* encode two SUN proteins (SUN1 and SUN2), that show a nuclear membrane location and play roles in nuclear division and DNA repair during blood stage of *P. falciparum* (Kandelis-Shalev et al., 2024). Another study on SUN1 in *P. berghei* show that it is localized on intranuclear body of the MTOC at the nuclear envelope that forms complex with Allantoicase and is essential for fertile male gamete formation (Sayers et al., 2024).

Plasmodium SUN1 shares some similarities with SUN proteins in other organisms like *S. cerevisiae and Schizosaccharomyces pombe* (Fan et al., 2022; Hagan and Yanagida, 1995), but its interaction with ALLAN is a highly specialized adaptation in *Plasmodium*. The location of SUN1 at the nuclear MTOC, distinct from axonemal markers like kinesin-8B, underscores its role in nuclear compartmentalization. Similarly, the absence of functional spindle formation and kinetochore attachment in *Δsun1* mutants is reminiscent of phenotypes seen in mutants of spindle-associated proteins in *Plasmodium*, such as EB1, ARK2 and kinesin-8X (Zeeshan et al., 2023; Zeeshan et al., 2019b). However, SUN1's role extends specifically to NE remodelling and the organization of the inner acentriolar MTOC.

Our study demonstrates that SUN1 is primarily localized to the nuclear side of the NE, forming dynamic loops and folds to accommodate the rapid expansion of the nucleus during three rounds of genome replication within 8 min. These loops serve as structural hubs for spindle assembly and kinetochore attachment at the nuclear MTOC, separating nuclear and cytoplasmic compartments. The absence of SUN1 disrupts spindle formation, causing defects in chromosome segregation and kinetochore attachment, while BB segregation remains incomplete, resulting in clumped basal bodies and anuclear flagellated gametes. This phenotype highlights the role of SUN1 in maintaining the nuclear compartment of the bipartite MTOC.

ALLAN, a novel allantoicase-like protein, has a location complementary to that of SUN1, forming focal points at the inner side of the NE. Unlike SUN1, ALLAN is present during other stages of *Plasmodium* mitosis, including schizogony and sporogony, suggesting a broader role in NE remodelling across the parasite's life cycle. Functional studies following ALLAN gene deletion revealed similar defects in MTOC organization, with impaired spindle formation, kinetochore attachment, and nuclear-cytoplasmic coordination. These findings indicate that SUN1 and ALLAN work together as a non-canonical LINC-like complex, replacing the role of lamins and KASH proteins in coordinating nuclear and cytoskeletal dynamics.

Interestingly, our interactome analysis identified kinesin-15 as a putative interactor of SUN1 and ALLAN, suggesting a possible link between this motor protein and nuclear remodelling. Previous studies have shown that kinesin-15 is essential for male gamete formation and is located partially at the plasma membrane and nuclear periphery, albeit mostly cytoplasmic (Zeeshan et al., 2022b). On the nuclear side, we found subunits of the condensin-II complex, similar to what was found in Arabidopsis(Ito et al., 2024; Sakamoto et al., 2022). These interaction with SUN1 and ALLAN raises the possibility of a broader network of proteins facilitating nuclear and cytoskeletal coordination during male gametogenesis.

Overall, these findings demonstrate that the SUN1-ALLAN complex plays a central role in integrating NE remodelling, spindle formation, and BB segregation during *Plasmodium* male gametogenesis. By acting as a functional substitute for the canonical LINC complex, SUN1 and ALLAN reflect the unique adaptations of apicomplexans to their rapid closed mitotic process.

Transcriptomic analysis of the *Δsun1* mutant showed significant upregulation of genes involved in lipid metabolism and microtubule organization. Lipidomic

profiling further confirmed substantial alterations in the lipid composition of SUN1-deficient gametocytes. Notably, PA and CE, both critical for membrane curvature and expansion, were reduced in the *Δsun1* mutant, whereas MAG and DAG levels were elevated. These disruptions likely reflect impaired NE expansion and structural integrity during gametogenesis. Additionally, the altered levels of specific fatty acids, such as arachidonic acid and myristic acid, suggest perturbations in both scavenged and apicoplast-derived lipid pathways.

The observed defects in NE dynamics in *Δsun1* gametocytes, including the absence of spindle formation and kinetochore attachment, can be attributed, in part, to these lipid imbalances. The inability of the NE to properly expand and maintain its structural integrity would disrupt its ability to accommodate the rapidly increasing ploidy during gametogenesis. This highlights the interconnectedness of NE remodelling and lipid metabolism in facilitating *Plasmodium*'s unique closed mitosis.

The interaction between SUN1 and ALLAN further emphasizes the role of this complex in NE-associated processes. While ALLAN primarily coordinates spindle and MTOC organization, its structural homology to galactose-binding domains raises the possibility of a lipid or glycan-binding function that could contribute to membrane homeostasis. Together, these findings suggest that the SUN1-ALLAN complex not only mediates structural NE remodelling but also integrates metabolic and biophysical processes essential for male gametogenesis.

The SUN1-ALLAN complex exemplifies a lineage-specific adaptation in *P. berghei*, highlighting the evolutionary plasticity of NE remodelling mechanisms across eukaryotes. SUN-domain proteins, a hallmark of LINC complexes, are widely conserved and diversified across eukaryotic lineages, yet *Plasmodium* and related apicomplexans lack key canonical LINC components.

Our analyses suggest that the SUN1-ALLAN complex is specific to Haemosporida. While SUN-domain proteins are conserved across most eukaryotes, the allantoicase-like protein ALLAN is a novel addition to the nuclear architecture of apicomplexans. Phylogenetic profiling indicates that ALLAN likely arose from a duplication of an allantoicase in an early apicomplexan ancestor, likely the ancestor to all coccidians and hematozoa. This event gave rise to two subtypes: AKiT8, associated with kinetochores (Brusini et al., 2022), and ALLAN, specialized in NE dynamics. Intriguingly, ALLAN is present not only during male gametogenesis but

also at other stages of the parasite's life cycle, including schizogony and sporogony, highlighting a potential broader role in *Plasmodium* NE remodelling.

The absence of KASH proteins and lamins in apicomplexans raises fascinating questions about how NE and cytoskeletal coordination evolved in this group. Comparative studies in ichthyosporeans, close relatives of fungi and animals, have identified intermediate forms of mitosis involving partial NE disassembly (Shah et al., 2024). In contrast, *Plasmodium* employs a highly streamlined closed mitosis, likely driven by the requirement for rapid nuclear and cytoskeletal coordination during male gametogenesis. The discovery of the SUN1-ALLAN axis suggests that apicomplexans have developed alternative strategies to adapt the NE for their cellular and mitotic requirements. These findings illustrate how *Plasmodium* has adapted its NE and MTOC architecture, highlighting the evolutionary flexibility of mitotic processes across eukaryotes, and raise intriguing questions about the evolutionary pressures that shaped this unique nuclear-cytoskeletal interface in apicomplexans. The presence of similar or other non-canonical complexes in other organisms remains an open question, with potential implications for understanding the diversity of mitotic processes.

This study opens several avenues for future research into the biology of the malaria parasite and its unique adaptations for mitosis. While the SUN1-ALLAN complex has been shown to play a central role in NE remodelling and bipartite MTOC coordination during male gametogenesis, many questions remain about its broader role and potential applications. Another key question concerns the evolutionary origins of the SUN1-ALLAN axis; comparative studies across apicomplexans, dinoflagellates, ciliates, and other non-model eukaryotes may help trace the evolution of this complex. The presence of similar non-canonical complexes in other rapidly dividing eukaryotic systems may shed light on the diversity of mitotic adaptations beyond *Plasmodium*. A functional further exploration of associated proteins, such as kinesin-15, may help elucidate how the SUN1-ALLAN complex integrates with other cellular machinery and structures. Investigating whether this motor protein directly interacts with SUN1 or ALLAN and has a catalytic role in nuclear-cytoskeletal remodelling may be critical to understand how the system achieves such rapid mitotic coordination. Finally, the work has translational potential. Targeting the SUN1-ALLAN complex and associated pathways is a novel approach to malaria transmission-blocking strategies. In conclusion, this work highlights some

remarkable innovations in *Plasmodium*'s mitotic machinery and provides the foundation for future research into both fundamental cell biology and therapeutic strategies.

Figure Legends

Fig 1. Location of SUN1 during male gametogenesis.

A. The upper panel schematic illustrates the process of male gametogenesis. N, genome ploidy. Live cell images show the location of SUN1-GFP (green) at different time points during male gametogenesis. DNA was stained with Hoechst. White arrows indicate the loop/folds. Representative images of more than 50 cells with more than three biological replicates. Scale bar: 5 µm. **B.** Serial block face-scanning electron microscopy (SBF-SEM) data slice of a gametocyte highlighting the complex morphology of the nucleus (cyan). Representative of more than 10 cells. Scale bar: 1 µm. **C.** Two 3D models of gametocyte nuclei showing their contorted and irregular morphology. Representative of more than 10 cells. Scale bar: 1 µm. **D.** Expansion microscopy (ExM) images showing location of SUN1 (green) detected with ant-GFP antibody and BB/MTOC stained with NHS ester (grey)**.** Hoechst was used to stain DNA. Scale bar 5 µm. Inset is the area marked with the red box around the BB/MTOC highlighted by NHS-ester staining. Scale bar: 1 µm. Representative images of more than 10 cells from two biological replicates. **E.** ExM images showing location of SUN1 (green) and α- tubulin (magenta) detected with ant-GFP and anti-tubulin antibodies, respectively**.** Hoechst was used to stain DNA. N=Nucleus; S=Spindle; A=Axoneme. Scale bar: 5 µm. Inset is the area marked with the white box on fig 1E middle panel around the BB/MTOC showing spindle and axoneme highlighted by tubulin staining. Scale bar: 1 µm. Representative images of more than 10 cells from two biological replicates. **F.** Live cell imaging showing location of SUN1-GFP (green) in relation to the BB and axoneme marker, kinesin-8B-mCherry (magenta) at different time points during gametogenesis. Blue in merged image is DNA stained with Hoechst. Representative images of more than 20 cells from more than three biological replicates. White arrows indicate the loop/folds of SUN1 where BB/axonemes are assembled outside the nuclear membrane. Scale bar: 5 µm. **G**. Live cell imaging showing location of SUN1-GFP (green) in relation to the spindle marker, EB1-mCherry (magenta) at different time points during gametogenesis. Blue in merged image is DNA stained with Hoechst. White arrows indicate the loop/folds of SUN1 where spindle poles and spindles are assembled inside the nuclear membrane. Representative images of more than 20 cells from more than three biological replicates. Scale bar: 5 µm. **H**. Live cell imaging showing location of

SUN1-GFP (green) in relation to the kinetochore marker, NDC80-mCherry (magenta) at different time points during gametogenesis. Blue in merged image is DNA stained with Hoechst. White arrows indicate the loop/folds of SUN1 where kinetochores are assembled inside the nuclear membrane. Representative images of more than 20 cells with more than three biological replicates. Scale bar: 5 µm.

Fig 2. Deletion of *sun1* affects male gamete formation and blocks parasite transmission.

A. Exflagellation centres per field at 15 min post-activation. n = 3 independent experiments (>10 fields per experiment). Error bar, ± SEM. **B.** Percentage ookinete conversion from zygote. n= 3 independent experiments (> 100 cells). Error bar, ± SEM. **C.** Total number of GFP-positive oocysts per infected mosquito in Δ*sun1* compared to WT-GFP parasites at 7-, 14- and 21-day post infection. Mean ± SEM. n= 3 independent experiments. **D.** Mid guts at 10x and 63x magnification showing oocysts of Δ*sun1* and WT-GFP lines at 7- and 21-day post infection. Scale bar: 50 µm in 10x and 20 µm in 63x. **E.** Rescue experiment showing *Δsun1* phenotype is due to defect in male *sun1* allele. Mean ± SEM. n= 3 independent experiments. **F, G.** Gene expression profile analysis using a volcano plot to highlight up- and downregulated genes in *Δsun1* compared to WT-GFP gametocytes activated for 8 min (F) and 30 min (G) respectively, with adjusted P-value cutoff of 0.05. **H, I.** Gene ontology enrichment analysis for upregulated genes in *Δsun1* compared to WT-GFP gametocytes, activated for 8 min (H) and 30 min (I) respectively. **J**. Schematic representation of lipid metabolism and membrane biogenesis. **K.** Comparative phospholipid profile of WTGFP and SUN1 gametocytes activated for 0 min and 8 min. The level of PA was significantly increased at 8-min post activation. **L.** Neutral lipid profiling shows significant increase in CE and MAG but not in TAG.

Fig 3. Ultrastructural analysis of *Δsun1* gametocytes showing defect in spindle formation and BB segregation

A. Deletion of *sun*1 blocks first spindle formation as observed by ExM of gametocytes activated for 1.5 min. α -tubulin: magenta, amine groups/NHS-ester reactive: shades of green. Basal Bodies: BB; spindle: S. Insets represent the zoomed area marked by the white boxes shown around BB/MTOC highlighted by NHS-ester and tubulin staining. Scale =5 µm

B. ExM images showing defect in BB/MTOC segregation in *Δsun1* gametocytes activated for 15 min. α -tubulin: magenta, amine groups/NHS-ester reactive: shades of green. Basal Bodies: BB; Insets represent the zoomed area shown around BB/MTOC highlighted by NHS-ester and tubulin staining. **C.** The schematic illustrates structures associated with mitosis and axoneme formation showing the first spindle is not formed, and BB are not separated in *Δsun1* gametocytes. More than 30 images were analysed in more than three different experiments. Scale bars = 5 µm. **D.** Electron micrographs of WT-GFP microgametocytes (male) at 8 min (**a-c**) and 15 min (**g, h**) plus *Δsun1* gametocytes at 8 min (**d-f**) and 15 min (**i-l**). Bars represent 1 µm (**a, d, i**), and 100 nm (**b, c, e, f, g, h, insert, j, k, l**).

a. Low power magnification of WT-GFP microgametocyte showing the central nucleus (N) with two nuclear poles (NP) with a basal body (BB) adjacent to one. The cytoplasm contains a number of axonemes (A).

b. Enlargement of enclosed area in **a** showing the basal body (BB) adjacent to one nuclear pole (NP).

c. Detail showing the close relationship between the nuclear pole (NP) and the basal body (BB). Note the cross-sectioned axonemes (A) showing the 9+2 microtubular arrangement.

d. Low power magnification of *Δsun1*showing a cluster of electron dense basal structures (enclosed area) in the cytoplasm adjacent to the nucleus (N). A – axonemes.

e. Detail from the cytoplasm shows a cluster of 4 basal bodies (arrowheads) and portions of axonemes (A) around central electron dense structure of nuclear pole (NP) material.

f. Detail from a nucleus showing kinetochores (K) with no attached microtubules.

g. Periphery of a flagellating microgamete showing the flagellum and nucleus protruding from the microgametocyte.

h. Detail of a longitudinally section of a microgamete showing the spiral relationship between the axoneme (A) and nucleus (N). **Insert.** Cross section of a microgamete showing 9+2 axoneme and adjacent nucleus (N).

i. Section through a microgametocyte with a central nucleus (N) undergoing exflagellation.

j. Enlargement of the enclosed area in **i** showing one cytoplasmic protrusion containing a single axoneme forming a flagellum (F), while the other has multiple axonemes (A)

k. Longitudinal section through a flagellum (F) with a basal body (B) at the anterior end but note the absence of a nucleus.

l. Cross section showing a cytoplasmic process contain 5 axonemes (A) but no associated nucleus.

E, F and G. Quantification of *Δsun1* phenotypes compared to WT-GFP during male gametogenesis. N = Nucleus; BB = Basal Body; NP = Nuclear pole; A = Axonemes.

Fig. 4. Reciprocal co-immunoprecipitation of PbSUN1-GFP and ALLAN-GFP during male gametogony

A. Projection of the first two components of a principal component analysis (PCA) of unique peptides derived from two SUN1-GFP (and WT-GFP immunoprecipitations with GFP-trap (peptide values: **Supplementary Table S2**). A subset of proteins is highlighted on the map based on relevant functional categories. **B.** Similar to panel A, but now for the allantoicase-like protein ALLAN (PBANKA_1304400). **C.** Selected proteins, their size and corresponding gene ID and representation by the number of peptides in either WT-GFP, PbSUN1-GFP and ALLAN-GFP precipitates.

Fig. 5. Localization of ALLAN-GFP during male gametogenesis

A. The schematic on upper panel illustrates the process of male gametogenesis. N, ploidy of nucleus**.** Live cell images showing the location of Allan-GFP (green) at different time points during male gametogenesis. Representative images of more than 50 cells with more than three biological replicates. Scale bar =5 µm. **B.** ExM images showing location of Allan-GFP (green) detected by anti-GFP antibody compared to spindle pole/MTOC and BB stained with NHS ester (grey) in gametocytes activated for 8 min. Scale bar =5 µm. Representative images of more than 20 cells with two biological replicates. Insets represent the zoomed area shown around SP/MTOC and BB highlighted by NHS-ester. Scale bar =1 µm. **C.** ExM images showing the location of Allan-GFP (green) compared to spindle and axonemes (magenta) detected by anti-GFP and ant-tubulin staining respectively in gametocytes activated for 8 min. Representative images of more than 20 cells with two biological replicates. Scale=5 µm. Insets represent the zoomed area shown

around spindle /axonemes highlighted by tubulin and GFP staining. Basal Bodies: BB; Spindle: S; Axonemes: A; Nucleus: N. Scale bar =1 µm. **D, E, F.** Live cell imaging showing location of Allan-GFP (green) in relation to the BB and axoneme marker, kinesin-8B-mCherry (magenta) (D); spindle marker, EB1-mCherry (magenta) (E); and kinetochore marker, NDC80-mCherry (magenta) (F) during first mitotic division (1-3 min) of male gametogenesis. Representative images of more than 20 cells with three biological replicates. Scale bar; 5 µm.

Fig. 6. Deletion of ALLAN impairs male gametogenesis by blocking BB segregation

A. Exflagellation centres per field at 15 min post-activation in *Δallan* compared to WT-GFP parasites. n≥3 independent experiments (>10 fields per experiment). Error bar, ± SEM. **B.** Percentage ookinete conversion from zygote. n≥3 independent experiments (> 100 cells). Error bar, ± SEM. **C.** Total number of GFP-positive oocysts per infected mosquito in *Δallan* compared to WT-GFP parasites at 7-, 14- and 21-day post infection. Mean ± SEM. n≥3 independent experiments. **D.** Total number of sporozoites in oocysts of *Δallan* compared to WT-GFP parasites at 14- and 21-day post infection. Mean ± SEM. n≥3 independent experiments. **E.** Total number of sporozoites in salivary glands of *Δallan* compared to WT-GFP parasites at 21-day post infection. Mean ± SEM. N=2 independent experiments. **F.** ExM images of gametocytes activated for 8- and 15- min showing MTOC/BB stained with NHS ester (green) and axonemes stained with anti-tubulin antibody (magenta). Axonemes: A; Basal Bodies: BB; Microtubule organising centre: MTOC. Insets represent the zoomed area shown around BB/MTOC highlighted by NHS-ester and tubulin staining. More than 30 images were analysed in more than three different experiments. Scale bars = 5 µm. **G.** Electron micrographs of WT-GFP microgametocytes at 8 mins (a-c) and 15 mins (d, e) and the *Δallan* at 8 min (f-h) and 15 min (I, j). Bars represent 1 µm (a, f) and 200 nm in all other images.

a. Low power of a microgametocyte showing the nucleus (N) with two nuclear pole complexes (arrows) consisting of the basal body, nuclear pole and attached kinetochores. Axonemes (A) are present in the cytoplasm.

b. Enlargement showing the nuclear pole (NP), associated basal body (BB) and axonemes (A).

c. Detail of the nuclear pole (NP) showing kinetochores (K) attached the spindle microtubules. Note the basal body (BB) adjacent to the nuclear pole (NP).

d. Longitudinal section of a microgamete showing the nucleus (N) closely associated with the axonemes (A).

e. Cross section through a microgamete showing the nucleus (N) and axoneme (A) enclosed plasma membrane.

f. Lower magnification of a microgametocyte showing a nucleus (N) with an adjacent clump of electron dense structures (enclosed area) and axonemes (A) in the cytoplasm.

g. Enlargement of the enclosed area in f showing multiple basal bodies (BB) and unseparated nuclear poles (NP) enclose by portions of nuclear membrane (NM). N – nucleus.

h. Detail from a nucleus showing several kinetochores (K) with no associated spindle microtubules.

i. Longitudinal section of an exflagellating cytoplasmic process consisting of two axonemes (A) but no nucleus.

j. Cross section through an exflagellating cytoplasmic process showing the presence of multiple axonemes (A) but the absence of any nucleus.

H to J. Quantification of *Δallan* phenotype compared to WT-GFP during male gametogenesis. N = Nucleus; BB = Basal Body; NP = Nuclear pole; A = Axonemes.

Fig 7. Evolution and Structure of the SUN1-ALLAN interaction A. Domain analysis shows two proteins with allantoicase domain and two proteins with sun-domain in *P. berghei.* The SUN domain and two domains comprising allantoicases are part of the same galactose-binding domain family, with a stikingly similar fold. **B.** Phylogenetic profiles showing the presence of SUN-, Allan- and KASH-domains and lamins proteins in Apicomplexa and a selection of other eukaryotes, including two model species *Homo sapiens* and *Arabidopsis thaliana.* **C.** AlphaFold3-modelled interaction between ALLAN and SUN1 based on separate domains (no full structure could be modelled). The SUN1 C-terminus forms a trimeric complex (pTM:0.37) similar to a trimeric ALLAN complex (grey) with the N-terminus of SUN1 interacting with ALLAN (pTM:0.55). This N-terminal domain is unique to Haemosporida. **D.** Overview of main interactors for putative localization at the nuclear envelope for ALLAN and SUN1 during male gametogenesis

Supplementary Figures and Tables

Supplementary Fig 1. Generation of PbSUN1-GFP/PbSUN1-mCherry parasites and analysis of subcellular location of SUN1-GFP during blood schizogony and gametogenesis

A. Schematic representation of the endogenous *sun1* locus, the GFP- and mCherry-tagging construct, and the recombined *sun1* locus following single homologous recombination. Arrows 1 and 2 indicate the position of PCR primers used to confirm successful integration of the construct. **B.** Diagnostic PCR of *sun1-GFP* and WT parasites using primers: integration primer (1) and ol492 (2). The band of expected size for amplified DNA fragment is indicated with arrow. **C.** Western blot showing expected size of SUN1-GFP fusion protein using anti-GFP antibody. The bands of expected size for control and Sun1-GFP are indicated with arrows. **D**. Diagnostic PCR of *sun1-mCherry* and WT parasites using primers: integration primer (1) and mCherry-P (2). The band of expected size for amplified DNA fragment is indicated with arrow. **E.** Live cell images of SUN1-GFP during blood schizogony showing no expression. DNA is stained with Hoechst dye (blue). Representative images of more than 50 cells with more than three biological replicates Scale; 5 μm. **F.** Live cell images of SUN1-GFP in male and female gametocytes. DNA is stained with Hoechst dye (blue). Representative images of more than 50 cells with more than three biological replicates Scale= 5 um. G. SBF-SEM data slices of a gametocyte highlighting the complex structure of the nucleus (cyan). Scale bar; 1 μm. **H.** Two 3D models of gametocyte nuclei showing its contorted and irregular morphology. Scale bar; 1 μm. I. SIM images of SUN1-GFP male gametocytes activated for different time points and fixed with paraformaldehyde. Representative images of more than 10 cells with more two biological replicates Scale; 1 μm.

Supplementary Fig 2. Localization of SUN1-GFP during various stages of parasite development.

A. Live cell imaging showing location of SUN1-GFP (green) in relation to the spindle marker, ARK2-mCherry (magenta) at different time points during male gametogenesis. DNA is stained with Hoechst dye (blue). Representative images of more than 20 cells with more than three biological replicates. Scale bar; 5 μm. **B.**

Live cell imaging showing location of SUN1-GFP (green) at different time points during female gametogenesis. DNA is stained with Hoechst dye (blue). Representative images of more than 20 cells with more than three biological replicates. Scale bar; 5 µm. **C**. Live cell images showing location of SUN1-GFP (green) in zygote and ookinete stages. A cy3-conjugated antibody, 13.1, which recognises the protein P28 on the surface of zygotes and ookinetes was used to mark these stages (magenta). DNA is stained with Hoechst dye (blue). Representative images of more than 20 cells with more than three biological replicates. Scale bar; 5 µm.

Supplementary Fig 3. Generation and genotype analysis of *sun1*-knockout (*Δsun1*) parasites.

A. Schematic representation of the endogenous *sun1* locus, the targeting knockout construct, and the recombined *sun1* locus following double homologous crossover recombination. Arrows 1 (P1) and 2 (P2) indicate PCR primers used to confirm successful integration in the *sun1* locus following recombination, and arrows 3 (P3) and 4 (P4) indicate PCR primers used to show deletion of the *sun1* gene. **B.** Integration PCR of the *sun1* locus in WTGFP (WT) and knockout (Mut) parasites using primers: integration primer (P1) and ol248 (P2). Integration of the targeting construct gives expected size band for each gene. **C**. qRT-PCR analysis showing deletion of *sun1* gene in *Δsun1* parasites compared to WTGFP. Mean ± SEM, n = 3 independent experiments. **D.** Bite back experiments reveal no transmission of *Δsun1* and successful transmission of WTGFP parasites from mosquito to mouse. Mean ± SEM. n = 3 independent experiments. **E-F.** RNA-seq analysis showing deletion of sun1 transcript in *Δsun1* gametocytes activated for 8- and 30-min. **G.** Comparative lysophosphatidylcholine (LPC) profile of WTGFP and SUN1 gametocytes activated for 0 min and 8 min. **H.** Comparative monoacylglycerol (MAG) profile of WTGFP and SUN1 gametocytes activated for 0 min and 8 min highlighting myristic acid (C14:0) and arachidonic acid (C20:3 and C20:4).

Supplementary Fig 4. Expansion Microscopy (ExM) shows defect in spindle formation and BB/MTOC segregation during male gametogenesis in *Δsun1* parasites

A. Deletion of *sun1* blocks first spindle formation as observed by ExM of gametocytes activated for 1.5 min. α -tubulin: magenta, amine groups/NHS-ester reactive: shades of grey. Basal Bodies: BB; spindle: S. Scale= 5 µm. **B.** ExM images showing defect in BB/MTOC segregation in gametocytes activated for 8 min. α -tubulin: magenta, amine groups/NHS-ester reactive: shades of grey. Basal Bodies: BB; Axoneme: A. Scale= 5 µm. **C.** ExM images showing defect in basal body/MTOC segregation in gametocytes activated for 15 min. α -tubulin: magenta, amine groups/NHS-ester reactive: shades of grey. Basal Bodies: BB; Axoneme: A. Scale= 5 µm.

Supplementary Fig 5. Transmission Electron Microscopy (TEM) reveals defect in BB/MTOC segregation and kinetochore attachment to spindle during male gametogenesis resulting in anucleated gamete formation in *Δsun1* parasites.

A. Electron micrographs of *Δsun1* gametocytes at 8 min **(a-c).** Enlargement showing cluster of electron dense basal bodies (BB)/nuclear poles (NPs) with associated axonemes (A) in the cytoplasm adjacent to a nucleus (N) **(b)** and detail from a nucleus showing kinetochores (K) with no attached microtubules connected NP **(c).** **B**. Electron micrographs of *Δsun1* gametocytes and flagella at 15 min **(a-l).** Enlargement showing a microtubule doublet that failed to assemble as classical 9+2 axonemes in the cytoplasm and detail from a nucleus showing kinetochores (K) with no attached microtubules **(b, c**). Another example of gametocyte **(d)** and enlargements showing axonemes attached separately with NP separately (**e, f**). Enlargement showing cluster of electron dense BB with associated axonemes (A) in the cytoplasm adjacent to a nucleus (N) (**h).** Another example of gametocyte and enlargement showing cluster of BB associated with axonemes (**j**). Cross section of an anucleate flagellum with quadruple axonemes **(k)** and longitudinal section of anucleated flagellum (**l). C**. Quantitative data for different phenotypes in *Δsun1* parasites compared to WT during male gametogenesis.

Supplementary Fig 6. Generation of PbALLAN-GFP parasites and analysis of subcellular location of PbALLAN-GFP during various stages of parasite life cycle

A. Schematic representation of the endogenous *allan* locus, the GFP-tagging construct, and the recombined *allan* locus following single homologous

recombination. Arrows 1 and 2 indicate the position of PCR primers used to confirm successful integration of the construct. **B.** Diagnostic PCR of ALLAN-GFP and WT parasites using primers: integration primer (1) and ol492 (2). The band of expected size for amplified DNA fragment is indicated with arrow. **C.** Western blot showing expected size of ALLAN-GFP fusion protein using anti-GFP antibody. The bands of expected size for control and Allan-GFP are indicated with arrows. **D.** Live cell images of ALLAN-GFP (green) during different stages of blood schizogony. Representative images of more than 50 cells with more than three biological replicates Scale; 5 µm. **E.** Live cell images of ALLAN-GFP (green) in activated gametocytes. Representative images of more than 50 cells with more than three biological replicates Scale; 5 µm. **F.** Live cell images of ALLAN-GFP (green) in zygote and ookinete. Representative images of more than 50 cells with more than three biological replicates Scale; 5 µm. **G.** Live cell images of ALLAN-GFP (green) during oocyst development and in sporozoite. Representative images of more than 50 cells with more than three biological replicates Scale; 5 µm. **H**. Live cell images of ALLAN-GFP (green) during liver stages. Representative images of more than 10 cells in two biological replicates Scale; 5 µm.

Supplementary Fig 7. Generation and genotype analysis of Pb*allan*-knockout (*Δallan*) parasites.

A. Schematic representation of the endogenous *allan* locus, the targeting knockout construct, and the recombined *allan* locus following double homologous crossover recombination. Arrows 1 (P1) and 2 (P2) indicate PCR primers used to confirm successful integration in the *allan* locus following recombination, and arrows 3 (P3) and 4 (P4) indicate PCR primers used to show deletion of the *allan* gene. **B.** Integration PCR of the *allan* locus in WTGFP (WT) and knockout (Mut) parasites using primers: integration primer (P1) and ol248 (P2). Integration of the targeting construct gives expected size band for each gene. **C**. qRT-PCR analysis showing deletion of *allan* gene in *Δallan* parasites compared to WTGFP. Mean ± SEM, n = 3 independent experiments. **D.** Bite back experiments reveal successful transmission of *Δallan* and WTGFP parasites from mosquito to mouse. Mean ± SEM. n = 3 independent experiments.

Supplementary Fig 8. TEM reveals defect in basal body/MTOC segregation and kinetochore attachment to spindle during male gametogenesis resulting in anucleate gamete formation in *Δallan* parasites

A. Electron micrographs of *Δallan* gametocytes at 8 min **(a-c).** Enlargement showing cluster of electron dense basal bodies (BB) with associated axonemes (A) in the cytoplasm adjacent to a nucleus (N) **(b)** and detail from a nucleus showing kinetochores (K) detached from nuclear pole (NP) **(c). B**. Electron micrographs of *Δallan* gametocytes and gametes at 15 min **(a-e)**. Enlargement showing cluster of electron dense BBs with associated axonemes (A) in the cytoplasm adjacent to a nucleus (N) (b). Example of gametocyte showing many spindle microtubules attached to NP (**c, d**). Longitudinal section of anucleate gamete (**e**). **C**. Quantitative data for different phenotypes in *Δallan* parasites compared to WT during male gametogenesis.

<u>Supplementary data</u>

Supplementary Table S1. List of genes differentially expressed between *Δsun1* and WT-GFP gametocytes.

RNA sequence analysis revealing the expression of various genes in *Δsun1* gametocytes in comparison to WT-GFP gametocytes activated for 8- and -15 min.

Supplementary Table S2. List of proteins and number of unique peptides for GFP-trap co-immunoprecipitants.

Spreadsheet (excel) file with unique peptide values for precipitates from lysates of gametocytes 8 min after activation for WT-GFP, SUN1-GFP and ALLAN-GFP parasites.

Supplementary Table S3. Phylogenetic analysis of SUN1, allantoicase-like, KASH and lamin proteins in Eukaryotes with a focus on Apicomplexa with sources for genomes (hyperlinks), sequences and IDs.

Supplementary Table S4. Oligonucleotides used in this study.

Methods

Ethics statement and mice details

The animal work passed an ethical review process and was approved by the United Kingdom Home Office. Work was carried out under UK Home Office Project Licenses (PDD2D5182 and PP3589958) in accordance with the UK 'Animals (Scientific Procedures) Act 1986'. Six- to eight-week-old female CD1 outbred mice from Charles River laboratories were used for all experiments. The conditions to keep the mice were a 12 h light and 12 h dark (7 am till 7 pm) cycle, the room temperature was kept between 20 and 24 °C and the humidity was kept between 40 and 60%.

Generation of transgenic parasites and genotype analyses

To generate GFP-tagged lines for SUN1, and ALLAN, a region of each gene downstream of the ATG start codon was amplified, ligated to the p277 vector, and transfected as previously described. The p277 vector includes a human DHFR cassette, providing resistance to pyrimethamine. Schematic representations of the endogenous gene loci, the constructs, and the recombined gene loci can be found in **Supplementary Figs. 1A and 6A**. For parasites expressing the C-terminal GFP-tagged proteins, diagnostic PCR was performed with primer 1 (Int primer) and primer 2 (ol492) to confirm integration of the GFP- and mCherry- targeting constructs **(Supplementary Figs. 1B and 6B)**. The primers used to generate the mutant parasite lines can be found in Supplementary Data 3.

Gene-deletion targeting vectors for SUN1, and ALLAN were created using the pBS-DHFR plasmid. This plasmid contains polylinker sites flanking a *Toxoplasma gondii* dhfr/ts expression cassette, which provides resistance to pyrimethamine, as previously described previously (Saini et al., 2017). To construct these vectors, PCR primers N1511 and N1512 were used to amplify a 1,1094 bp fragment of the 5′ upstream sequence to *sun1* from genomic DNA, which was then inserted into the ApaI and HindIII restriction sites upstream of the dhfr/ts cassette in the pBS-DHFR plasmid. A 776 bp fragment from the 3′ flanking region of *sun1* gene generated with primers N1513 and N1514, was inserted downstream of the dhfr/ts cassette using EcoRI and XbaI restriction sites. The same method was applied for *allan* amplifying the upstream (1044 bp) and downstream (1034 bp) sequences and inserted to pBS-DHFR plasmid. The linear targeting sequence was released using *Apa*I/*Xba*I. A schematic representation of the endogenous *sun1* and *allan* loci, the construct and

the recombined *sun1* and *allan* loci can be found in Supplementary Fig. 1A and 6A respectively. The primers used to generate the mutant parasite lines can be found in **Supplementary Table S4**. A diagnostic PCR was used with primer 1 (IntN151_5) and primer 2 (ol248) to confirm integration of the targeting construct, and primer 3 (Int303) and primer 4 (N1514) were used to confirm deletion of the *sun1* gene **(Supplementary Fig. S1B** and **Supplementary Table S4)**. Similarly, a diagnostic PCR was used with primer 1 (IntN153_5) and primer 2 (ol248) to confirm integration of the targeting construct, and primer 3 (Int307) and primer 4 (N1534) were used to confirm deletion of the *allan* gene **(Supplementary Fig. S6B and Supplementary Table S4)**. *P. berghei* ANKA line 2.34 (for GFP-and mCherry-tagging) or ANKA line 507cl1 expressing GFP (for the gene-deletion and knockdown construct) parasites were transfected by electroporation (Janse et al., 2006).

Purification of schizonts and gametocytes

Blood cells obtained from infected mice (day 4 post infection) were cultured for 11 h and 24 h at 37°C (with rotation at 100 rpm) and schizonts were purified the following day on a 60% v/v NycoDenz (in phosphate-buffered saline (PBS)) gradient, (NycoDenz stock solution: 27.6% w/v NycoDenz in 5 mM Tris-HCl (pH 7.20), 3 mM KCl, 0.3 mM EDTA).

Gametocytes were purified using a modified version of the protocol by Beetsma et al. (1998). In brief, parasites were injected into mice pre-treated with phenylhydrazine and enriched by sulfadiazine treatment two days post-infection. Blood was collected on the fourth day post-infection, and gametocyte-infected cells were purified using a 48% NycoDenz gradient (prepared with 27.6% NycoDenz in PBS, containing 5 mM Tris–HCl, pH 7.20, 3 mM KCl, and 0.3 mM EDTA). Gametocytes were harvested from the interface of the gradient and washed thoroughly.

Live-cell imaging

To investigate SUN1-GFP, and ALLAN-GFP expression during erythrocytic stages, parasites cultured in schizont medium were imaged at various stages of schizogony. Purified gametocytes were assessed for GFP expression and location at different time points (0, 1 to 15 minutes) post-activation in ookinete medium (RPMI medium 1640, 100 µM xanthurenic acid, 1% w/v sodium bicarbonate, 20 % v/v heat-inactivated FBS. Zygote and ookinete stages were examined over a 24-hour culture

period using the cy3-conjugated 13.1 antibody (red), which targets the P28 protein on the surface of zygotes and ookinetes. Oocysts and sporozoites were imaged in the infected mosquito guts. All images were captured with a 63× oil immersion objective on a Zeiss AxioImager M2 microscope equipped with an AxioCam ICc1 digital camera.

Western blot analysis

Purified gametocytes were placed in lysis buffer (10 mM Tris-HCl [pH 7.5], 150 mM NaCl, 0.5 mM EDTA, and 1% NP-40). The lysed samples were boiled for 10 min at 95°C after adding Laemmli buffer and then centrifuged at maximum speed (13,000 g) for 5 min. The samples were electrophoresed on a 4% to 12% SDS-polyacrylamide gel. Subsequently, resolved proteins were transferred to nitrocellulose membrane (Amersham Biosciences). Immunoblotting was performed using the Western Breeze Chemiluminescence Anti-Rabbit kit (Invitrogen) and anti-GFP polyclonal antibody (Invitrogen) at a dilution of 1:1,250, according to the manufacturer's instructions.

Generation of dual tagged parasite lines

The GFP (green)-tagged SUN1 or ALLAN parasite lines were mixed with mCherry (red)-tagged lines of kinetochore marker (NDC80), basal body/axoneme marker (kinesin-8B), and spindle markers (EB1 and ARK2) in equal numbers and injected into mice. Mosquitoes were fed on these mice 4 to 5 days post-infection, when gametocytaemia was high, and were monitored for oocyst development and sporozoite formation at days 14 and 21 after feeding. Infected mosquitoes were then allowed to feed on naïve mice, and after 4 to 5 days, the mice were examined for blood-stage parasitaemia using microscopy with Giemsa-stained blood smears. This process resulted in some parasites expressing both GFP and mCherry in the resultant gametocytes. These gametocytes were then purified, and fluorescence microscopy images were collected as previously described.

Parasite phenotype analyses

Blood samples containing approximately 50,000 parasites of the SUN1-knockout, and ALLAN-knockout lines were injected intraperitoneally (i.p.) into mice to initiate infection. Asexual stages and gametocyte production were monitored using

microscopy on Giemsa-stained thin smears. Four to five days post-infection, exflagellation and ookinete conversion were examined as previously described, using a Zeiss AxioImager M2 microscope (Carl Zeiss, Inc.) equipped with an AxioCam ICc1 digital camera.

To analyze mosquito infection and transmission, 30 to 50 *Anopheles stephensi* SD 500 mosquitoes were allowed to feed for 20 min on anesthetized, infected mice with at least 15% asexual parasitaemia and comparable gametocyte levels, as determined by Giemsa-stained blood films. To assess midgut infection, approximately 15 guts were dissected from mosquitoes on days 7 and 14 post-feeding, and oocysts were counted using a 63× oil immersion objective. On day 21 post-feeding, another 20 mosquitoes were dissected, and their guts and salivary glands were separately crushed in a loosely fitting homogenizer to release sporozoites, which were then quantified using a haemocytometer or used for imaging.

Mosquito bite-back experiments were conducted 21 days post-feeding using naive mice, and blood smears were examined after 3 to 4 days.

Immunoprecipitation and Mass Spectrometry

Male gametocytes of SUN1-GFP, and ALLAN-GFP parasites were used at 6-min post-activation to prepare cell lysates. WT-GFP gametocytes were used as controls. Purified parasite pellets were cross-linked using formaldehyde (10 min incubation with 1% formaldehyde, followed by 5 min incubation in 0.125 M glycine solution and three washes with phosphate-buffered saline [PBS; pH 7.5]). Immunoprecipitation was conducted using the protein lysates and a GFP-Trap_A Kit (Chromotek) according to the manufacturer's instructions. Briefly, lysates were incubated for 2 hours with GFP-Trap_A beads at 4°C with continuous rotation. Unbound proteins were washed away, and proteins bound to the beads were digested using trypsin. The tryptic peptides were analyzed by liquid chromatography-tandem mass spectrometry. Mascot (http://www.matrixscience.com/) and MaxQuant (https://www.maxquant.org/) search engines were used for mass spectrometry data analysis. Experiments were performed in duplicate. Peptides and proteins with a minimum threshold of 95% were used for further proteomic analysis. The PlasmoDB database was used for protein annotation, and a separate manual curation was performed to classify proteins into categories relevant for SUN1/ALLAN pulldowns:

chromatin, nuclear pore, ER membrane and axonemal proteins. To capture co-variation of pulldown proteins between different experiments (GFP-only versus SUN1-GFP ALLAN-GFP) we performed principal component analysis (PCA) using unique peptide values per protein present in two replicates per experiment. Values for undetected proteins were set to 0. Values were ln (x+1) transformed and PCA was performed using the ClustVis webserver (settings Nipals PCA, no scaling) (Metsalu and Vilo, 2015).

AlphaFold3 modelling

3D protein structures SUN1 and ALLAN were modelled using the AlphaFold3 webserver (https://alphafoldserver.com/) with standard settings (seed set to 100) (Abramson et al., 2024). To assess the stoichiometry of the complex we attempted monomers up to decamers for both ALLAN and SUN1, using both the N-terminus, middle domain and C-terminus of SUN1. ALLAN consistent formed higher order structures containing trimeric complexes. SUN1 could form higher order structures beyond trimers but given the trimer of ALLAN we opted for modelling SUN1 as a trimer as well.

Fixed Immunofluorescence Assay

SUN1-KO and ALLAN-KO gametocytes were purified, activated in ookinete medium, fixed at various time points with 4% paraformaldehyde (PFA, Sigma) diluted in microtubule (MT)-stabilizing buffer (MTSB) for 10–15 min, and added to poly-L-lysine coated slides. Immunocytochemistry used primary mouse anti-α tubulin mAb (Sigma-T9026; used at 1:1000), and secondary antibody was Alexa 488 conjugated anti-mouse IgG (Invitrogen-A11004) (used at 1:1000). The slides were then mounted in Vectashield with DAPI (Vector Labs) for fluorescence microscopy. Parasites were visualized on a Zeiss AxioImager M2 microscope fitted with an AxioCam ICc1 digital camera.

Liver stage cultures

Human liver hepatocellular carcinoma (HepG2) cells (European Cell Culture Collection) were grown in DMEM medium, supplemented with 10% heat inactivated foetal bovine serum, 0.2% $NaHCO_3$, 1% sodium pyruvate, 1% penicillin/streptomycin and 1% L-glutamine in a humidified incubator at 37°C with 5% CO2. For infection,

1×10^5 HepG2 cells were seeded in a 48-well culture plate. The day after seeding, salivary glands were removed from female *Anopheles stephensi* mosquitoes infected with PbALLAN-GFP parasites and following mechanical disruption, sporozoites were purified and added in infection medium. The culture was maintained for 72 h.

Ultrastructure Expansion Microscopy (UExM)

Purified gametocytes were activated for different time points, and activation was stopped by adding 4% paraformaldehyde. Fixed samples were then attached to a 12 mm round poly-D-lysine (A3890401, Gibco) coated coverslip for 10 min. Coverslips were incubated overnight in 1.4% formaldehyde (FA)/2% acrylamide (AA) at 4°C. Gelation was performed in ammonium persulfate (APS)/Temed (10% each)/monomer solution (23% sodium acrylate; 10% AA; 0.1% BIS-AA in PBS) for 1 h at 37°C. Gels were denatured for 15 min at 37°C and 45 min at 95°C. After denaturation, gels were incubated in distilled water overnight for complete expansion. The following day, gels were washed twice in PBS for 15 min to remove excess of water. Gels were then incubated with primary antibodies at 37°C for 3 h and washed 3 times for 10 min in PBS/ 0.1% Tween. Incubation with secondary antibodies was performed for 3 h at 37°C followed by 3 washes of 10 min each in PBS/ 0.1% Tween (all antibody incubation steps were performed with 120 to 160 rpm shaking at 37°C). Directly after antibody staining, gels were incubated in 1 ml of 594 NHS-ester (Merck: 08741) diluted at 10 µg/ml in PBS for 1 h and 30 min at room temperature on a shaker. The gels were then washed 3 times for 15 min with PBS/0.1% Tween and expanded overnight in ultrapure water. Gel pieces of 1 cm × 1 cm were cut from the expanded gel and attached to 24 mm round Poly-D-Lysine (A3890401, Gibco) coated coverslips to prevent the gel from sliding and to avoid drifting while imaging. Immuno-labelling used primary antibody against α-tubulin (1:1000 dilution, Sigma-T9026), and anti-GFP antibody (1:250, Thermo Fisher). Secondary antibodies, anti-rabbit Alexa 488, and anti-mouse Alexa 568 were used at dilutions of 1:1000 (Invitrogen). Atto 594 NHS-ester was used for bulk proteome labelling (Merck 08741). Images were acquired on Zeiss Elyra PS.1-LSM780 and CD7-LSM900 and Airyscan confocal microscopes, where 0.4 Airy unit (AU) on confocal and 0.2 AU were used along with slow scan modes. Image analysis was performed using Zeiss Zen 2012 Black edition and Fiji-Image J.

Structured Illumination Microscopy

A small volume (3 µl) of gametocytes suspension was placed on a microscope slide and covered with a long (50 × 34 mm) coverslip to obtain a very thin monolayer and immobilize the cells. Cells were scanned with an inverted microscope using a Zeiss Plan-Apochromat 63x/1.4 oil immersion or Zeiss C-Apochromat 63x/1.2 W Korr M27 water immersion objective on a Zeiss Elyra PS.1 microscope, utilizing the structured illumination microscopy (SIM) technique. The correction collar of the objective was set to 0.17 for optimal contrast. The following settings were used in SIM mode: lasers, 405 nm: 20%, 488 nm: 16%; exposure times 200 ms (Hoechst), 100 ms (GFP), three grid rotations, five phases. The bandpass filters BP 420-480 + LP 750, and BP 495-550 + LP 750 were used for the blue and green channels, respectively. Where multiple focal planes (Z-stacks) were recorded processing and channel alignment was done as described previously (Zeeshan et al., 2024).

Electron microscopy

Gametocytes activated for 8 min and 15 min were fixed in 4% glutaraldehyde in 0.1 M phosphate buffer and processed for electron microscopy (Ferguson et al., 2005). Briefly, samples were post fixed in osmium tetroxide, treated en bloc with uranyl acetate, dehydrated and embedded in Spurr's epoxy resin. Thin sections were stained with uranyl acetate and lead citrate prior to examination in a JEOL JEM-1400 electron microscope (JEOL, United Kingdom). The experiments were done at least 3 times to capture every stage of the parasite, and 50 to 55 cells were analysed for the phenotype. For more details, please see the figure legends.

RNA Isolation and Quantitative Real-Time PCR (qRT-PCR) Analyses

RNA was extracted from purified gametocytes using an RNA purification kit (Stratagene). Complementary DNA (cDNA) was synthesized using an RNA-to-cDNA kit (Applied Biosystems). Gene expression was quantified from 80 ng of total RNA using the SYBR Green Fast Master Mix kit (Applied Biosystems). All primers were designed using Primer3 (Primer-BLAST, NCBI). The analysis was conducted on an Applied Biosystems 7500 Fast machine with the following cycling conditions: 95°C for 20 sec, followed by 40 cycles of 95°C for 3 sec and 60°C for 30 sec. Three technical replicates and three biological replicates were performed for each gene tested. The genes hsp70 (PBANKA_081890) and arginyl-tRNA synthetase

(PBANKA_143420) were used as endogenous control reference genes. The primers used for qPCR are listed in **Supplementary Table S4**.

RNA-seq Analysis

Libraries were prepared from lyophilized total RNA, starting with the isolation of mRNA using the NEBNext Poly(A) mRNA Magnetic Isolation Module (NEB), followed by the NEBNext Ultra Directional RNA Library Prep Kit (NEB) as per the manufacturer's instructions. Libraries were amplified through 12 PCR cycles (12 cycles of [15 s at 98°C, 30 s at 55°C, 30 s at 62°C]) using the KAPA HiFi HotStart Ready Mix (KAPA Biosystems). Sequencing was performed on a NovaSeq 6000 DNA sequencer (Illumina), generating paired-end 100-bp reads.

FastQC [https://www.bioinformatics.babraham.ac.uk/projects/fastqc/ was used to analyze raw read quality and the adapter sequences were removed using Trimmomatic (v0.39) [http://www.usadellab.org/cms/?page=trimmomatic]. The resulting reads were mapped against the P. *berghei* genome (PlasmoDB, v68) using HISAT2 (v2-2.2.1) with the --very-sensitive parameter. Uniquely mapped, properly paired reads with mapping quality of 40 or higher were retained using SAMtools (v1.19) [http://samtools.sourceforge.net/]. Raw read counts were determined for each gene in the *P. berghei* genome using BedTools [https://bedtools.readthedocs.io/en/latest/ #] to intersect the aligned reads with the genome annotation. Differential expression analysis was performed using DESeq2 to call up-and down-regulated genes (FDR < 0.05 and log2 FC > 1.0). Volcano plots were made using the R package Enhanced Volcano.

Statistical Analysis

All statistical analyses were conducted using GraphPad Prism 9 (GraphPad Software). Student's t-test and/or a two-way ANOVA test were employed to assess differences between control and experimental groups. Statistical significance is indicated as *P < 0.05, **P < 0.01, ***P < 0.001, or ns for not significant. 'n' denotes the sample size in each group or the number of biological replicates. For qRT-PCR data, a multiple comparisons t-test, with post hoc Holm–Sidak test, was utilized to evaluate significant differences between wild-type and mutant strains.

Data availability

The RNA-seq data generated in this study have been deposited in the NCBI Sequence Read Archive. Mass spectrometry proteomics data have been deposited to the ProteomeXchange Consortium via the PRIDE partner repository. Source data are provided with this paper.

Acknowledgements

R.T. is supported by ERC advance grant funded by UKRI Frontier Science (EP/X024776/1), MRC UK (MR/K011782/1) and BBSRC (BB/L013827/1, BB/X014681/1). M.Z, I.B., D.B. A.M. were supported as research fellows by (EP/X024776/1). R.Y. is supported by BBSRC (BB/X014681/1). S.L.P is supported by Wellcome DBT India Alliance/Team Science (IA/TSG/21/1/600261). AAH is supported by the Francis Crick Institute (FC001097), which receives core funding from the Cancer Research UK (FC001097), the UK Medical Research Council (FC001097), and the Wellcome Trust (FC001097). KGLR is supported by the NIH/NIAID (R01 AI136511) and the University of California, Riverside (NIFA-Hatch-225935. E.T. is supported by a personal fellowship from the Nederlandse Organisatie voor Wetenschappelijk Onderzoek, the Netherlands (grant no. VI. Veni.202.223). YYB and CYB were supported by Agence Nationale de la Recherche, France (Project ApicoLipiAdapt grant ANR-21-CE44-0010 ; Project Apicolipidtraffic grant ANR-23-CE15-0009-01 ; Project OIL grant ANR-24-CE15-2171-02), The Fondation pour la Recherche Médicale (FRM EQU202103012700), Laboratoire d'Excellence Parafrap, France (grant ANR-11-LABX-0024), LIA-IRP CNRS Program (Apicolipid project), the Université Grenoble Alpes (IDEX ISP Apicolipid) and Région Auvergne Rhone-Alpes for the lipidomics analyses platform (Grant IRICE Project GEMELI), Collaborative Research Program Grant CEFIPRA (Project 6003-1) by the CEFIPRA (MESRI-DBT). Confocal and SIM microscopy was conducted in the School of Life Sciences Imaging (SLIM). For Open Access, the authors have applied a CC BY public copyright licence to any Author Accepted Manuscript version arising from this submission. We thank Cleidiane Zampronio at Warwick University for mass spectrometry methods and Bio Support Unit, University of Nottingham for maintenance of mice used in this study.

Contributions

R.T. conceived and coordinated the project; M.Z., I.B. and R.T. performed and analysed the live-cell imaging, knockout, and proteomics data; M.Z., R.T., I.B. and D.B. performed mice and mosquito-related work; R.Y. and D.J.P.F performed and analysed electron microscopy imaging. M.Z., S.L.P. and R.Y. performed expansion microscopy; Z.C., B.M. and S.B. performed RNA-seq analysis; Y.Y.B. and C.Y.B. did lipid analysis; A.M. performed liver stage microscopy; M.H., D.J.P.F. and S.V. performed SBF-SEM and 3D nuclear modelling. R.M. performed structured illumination microscopy; I.B. and D.B. performed qRT PCRs; A.B. performed mass spectrometry analysis; E.C.T. performed the interactomics, structural and phylogenetic analyses; S. B. performed, structural analyses; R.T., and A.A.H. supervised the project; M.Z., D.B. and R.T. managed the project. M.Z. E.C.T. and R.T. prepared the first manuscript draft. A.A.H. helped significantly in editing and writing and all authors contributed to manuscript editing and revisions.

Competing interests

The authors declare no competing interests.

References

Abramson, J., Adler, J., Dunger, J., Evans, R., Green, T., Pritzel, A., Ronneberger, O., Willmore, L., Ballard, A.J., Bambrick, J.*, et al.* (2024). Accurate structure prediction of biomolecular interactions with AlphaFold 3. Nature *630*, 493-500.

Amiar, S., Katris, N.J., Berry, L., Dass, S., Duley, S., Arnold, C.S., Shears, M.J., Brunet, C., Touquet, B., McFadden, G.I.*, et al.* (2020). Division and Adaptation to Host Environment of Apicomplexan Parasites Depend on Apicoplast Lipid Metabolic Plasticity and Host Organelle Remodeling. Cell Rep *30*, 3778-3792 e3779.

Baum, D.A., and Baum, B. (2014). An inside-out origin for the eukaryotic cell. BMC Biol *12*, 76.

Boettcher, B., and Barral, Y. (2013). The cell biology of open and closed mitosis. Nucleus *4*, 160-165.

Botte, C.Y., Yamaryo-Botte, Y., Rupasinghe, T.W., Mullin, K.A., MacRae, J.I., Spurck, T.P., Kalanon, M., Shears, M.J., Coppel, R.L., Crellin, P.K.*, et al.* (2013). Atypical lipid composition in the purified relict plastid (apicoplast) of malaria parasites. Proc Natl Acad Sci U S A *110*, 7506-7511.

Brusini, L., Dos Santos Pacheco, N., Tromer, E.C., Soldati-Favre, D., and Brochet, M. (2022). Composition and organization of kinetochores show plasticity in apicomplexan chromosome segregation. J Cell Biol *221*.

Dey, G., and Baum, B. (2021). Nuclear envelope remodelling during mitosis. Curr Opin Cell Biol *70*, 67-74.

Dubois, D., Fernandes, S., Amiar, S., Dass, S., Katris, N.J., Botte, C.Y., and Yamaryo-Botte, Y. (2018). Toxoplasma gondii acetyl-CoA synthetase is involved in fatty acid elongation (of long fatty acid chains) during tachyzoite life stages. J Lipid Res *59*, 994-1004.

Fan, J., Sun, Z., and Wang, Y. (2022). The assembly of a noncanonical LINC complex in Saccharomyces cerevisiae. Curr Genet *68*, 91-96.

Ferguson, D.J., Henriquez, F.L., Kirisits, M.J., Muench, S.P., Prigge, S.T., Rice, D.W., Roberts, C.W., and McLeod, R.L. (2005). Maternal inheritance and stage-specific variation of the apicoplast in Toxoplasma gondii during development in the intermediate and definitive host. Eukaryot Cell *4*, 814-826.

Graumann, K., Vanrobays, E., Tutois, S., Probst, A.V., Evans, D.E., and Tatout, C. (2014). Characterization of two distinct subfamilies of SUN-domain proteins in Arabidopsis and their interactions with the novel KASH-domain protein AtTIK. J Exp Bot *65*, 6499-6512.

Guttery, D.S., Zeeshan, M., Ferguson, D.J.P., Holder, A.A., and Tewari, R. (2022). Division and Transmission: Malaria Parasite Development in the Mosquito. Annu Rev Microbiol *76*, 113-134.

Hagan, I., and Yanagida, M. (1995). The product of the spindle formation gene sad1+ associates with the fission yeast spindle pole body and is essential for viability. J Cell Biol *129*, 1033-1047.

Hao, H., and Starr, D.A. (2019). SUN/KASH interactions facilitate force transmission across the nuclear envelope. Nucleus *10*, 73-80.

Ito, N., Sakamoto, T., Oko, Y., Sato, H., Hanamata, S., Sakamoto, Y., and Matsunaga, S. (2024). Nuclear pore complex proteins are involved in centromere distribution. iScience *27*, 108855.

Janse, C.J., Ramesar, J., and Waters, A.P. (2006). High-efficiency transfection and drug selection of genetically transformed blood stages of the rodent malaria parasite Plasmodium berghei. Nat Protoc *1*, 346-356.

Kandelis-Shalev, S., Goyal, M., Assaraf, S., Elam, T., Dahan, N., Berenshtein, E., and Dzikowski, R. (2024). SUN-domain proteins of the malaria parasite Plasmodium falciparum are essential for

proper nuclear division and DNA repair BioRxiv.

Koreny, L., and Field, M.C. (2016). Ancient Eukaryotic Origin and Evolutionary Plasticity of Nuclear Lamina. Genome Biol Evol *8*, 2663-2671.

Liu, S., and Pellman, D. (2020). The coordination of nuclear envelope assembly and chromosome segregation in metazoans. Nucleus *11*, 35-52.

Makarova, M., and Oliferenko, S. (2016). Mixing and matching nuclear envelope remodeling and spindle assembly strategies in the evolution of mitosis. Curr Opin Cell Biol *41*, 43-50.

Metsalu, T., and Vilo, J. (2015). ClustVis: a web tool for visualizing clustering of multivariate data using Principal Component Analysis and heatmap. Nucleic Acids Res *43*, W566-570.

Rout, M.P., Obado, S.O., Schenkman, S., and Field, M.C. (2017). Specialising the parasite nucleus: Pores, lamins, chromatin, and diversity. PLoS Pathog *13*, e1006170.

Saini, E., Zeeshan, M., Brady, D., Pandey, R., Kaiser, G., Koreny, L., Kumar, P., Thakur, V., Tatiya, S., Katris, N.J.*, et al.* (2017). Photosensitized INA-Labelled protein 1 (PhIL1) is novel component of the inner membrane complex and is required for Plasmodium parasite development. Sci Rep *7*, 15577.

Sakamoto, T., Sakamoto, Y., Grob, S., Slane, D., Yamashita, T., Ito, N., Oko, Y., Sugiyama, T., Higaki, T., Hasezawa, S.*, et al.* (2022). Two-step regulation of centromere distribution by condensin II and the nuclear envelope proteins. Nat Plants *8*, 940-953.

Sayers, C., Pandey, V., Balakrishnan, A., Michie, K., Svedberg, D., Hunziker, M., Pardo, M., Choudhary, J., Berntsson, R., and Billker, O. (2024). Systematic screens for fertility genes essential for malaria parasite transmission reveal conserved aspects of sex in a divergent eukaryote. Cell Syst *15*, 1075-1091 e1076.

Sazer, S., Lynch, M., and Needleman, D. (2014). Deciphering the evolutionary history of open and closed mitosis. Curr Biol *24*, R1099-1103.

Shah, H., Olivetta, M., Bhickta, C., Ronchi, P., Trupinic, M., Tromer, E.C., Tolic, I.M., Schwab, Y., Dudin, O., and Dey, G. (2024). Life-cycle-coupled evolution of mitosis in close relatives of animals. Nature *630*, 116-122.

Shunmugam, S., Arnold, C.S., Dass, S., Katris, N.J., and Botte, C.Y. (2022). The flexibility of Apicomplexa parasites in lipid metabolism. PLoS Pathog *18*, e1010313.

Sinden, R.E., Canning, E.U., Bray, R.S., and Smalley, M.E. (1978). Gametocyte and gamete development in Plasmodium falciparum. Proc R Soc Lond B Biol Sci *201*, 375-399.

Sinden, R.E., Talman, A., Marques, S.R., Wass, M.N., and Sternberg, M.J. (2010). The flagellum in malarial parasites. Curr Opin Microbiol *13*, 491-500.

Smoyer, C.J., and Jaspersen, S.L. (2014). Breaking down the wall: the nuclear envelope during mitosis. Curr Opin Cell Biol *26*, 1-9.

Starr, D.A., and Fridolfsson, H.N. (2010). Interactions between nuclei and the cytoskeleton are mediated by SUN-KASH nuclear-envelope bridges. Annu Rev Cell Dev Biol *26*, 421-444.

Tzur, Y.B., Wilson, K.L., and Gruenbaum, Y. (2006). SUN-domain proteins: 'Velcro' that links the nucleoskeleton to the cytoskeleton. Nat Rev Mol Cell Biol *7*, 782-788.

Wagner, M., Song, Y., Jimenez-Ruiz, E., Hartle, S., and Meissner, M. (2023). The SUN-like protein TgSLP1 is essential for nuclear division in the apicomplexan parasite Toxoplasma gondii. J Cell Sci *136*.

Zeeshan, M., Brady, D., Markus, R., Vaughan, S., Ferguson, D., Holder, A.A., and Tewari, R. (2022a). Plasmodium SAS4: basal body component of male cell which is dispensable for parasite transmission. Life Sci Alliance *5*.

Zeeshan, M., Ferguson, D.J., Abel, S., Burrrell, A., Rea, E., Brady, D., Daniel, E., Delves, M., Vaughan, S., Holder, A.A.*, et al.* (2019a). Kinesin-8B controls basal body function and flagellum formation and is key to malaria transmission. Life Sci Alliance *2*.

Zeeshan, M., Pandey, R., Ferguson, D.J.P., Tromer, E.C., Markus, R., Abel, S., Brady, D., Daniel, E., Limenitakis, R., Bottrill, A.R.*, et al.* (2020). Real-time dynamics of Plasmodium NDC80 reveals unusual modes of chromosome segregation during parasite proliferation. J Cell Sci *134*.

Zeeshan, M., Rashpa, R., Ferguson, D.J., McKeown, G., Nugmanova, R., Subudhi, A.K., Beyeler, R., Pashley, S.L., Markus, R., Brady, D.*, et al.* (2024). Plasmodium

NEK1 coordinates MTOC organisation and kinetochore attachment during rapid mitosis in male gamete formation. PLoS Biol *22*, e3002802.

Zeeshan, M., Rashpa, R., Ferguson, D.J.P., Abel, S., Chahine, Z., Brady, D., Vaughan, S., Moores, C.A., Le Roch, K.G., Brochet, M.*, et al.* (2022b). Genome-wide functional analysis reveals key roles for kinesins in the mammalian and mosquito stages of the malaria parasite life cycle. PLoS Biol *20*, e3001704.

Zeeshan, M., Rea, E., Abel, S., Vukusic, K., Markus, R., Brady, D., Eze, A., Rashpa, R., Balestra, A.C., Bottrill, A.R.*, et al.* (2023). Plasmodium ARK2 and EB1 drive unconventional spindle dynamics, during chromosome segregation in sexual transmission stages. Nat Commun *14*, 5652.

Zeeshan, M., Shilliday, F., Liu, T., Abel, S., Mourier, T., Ferguson, D.J.P., Rea, E., Stanway, R.R., Roques, M., Williams, D.*, et al.* (2019b). Plasmodium kinesin-8X associates with mitotic spindles and is essential for oocyst development during parasite proliferation and transmission. PLoS Pathog *15*, e1008048.

Fig 1

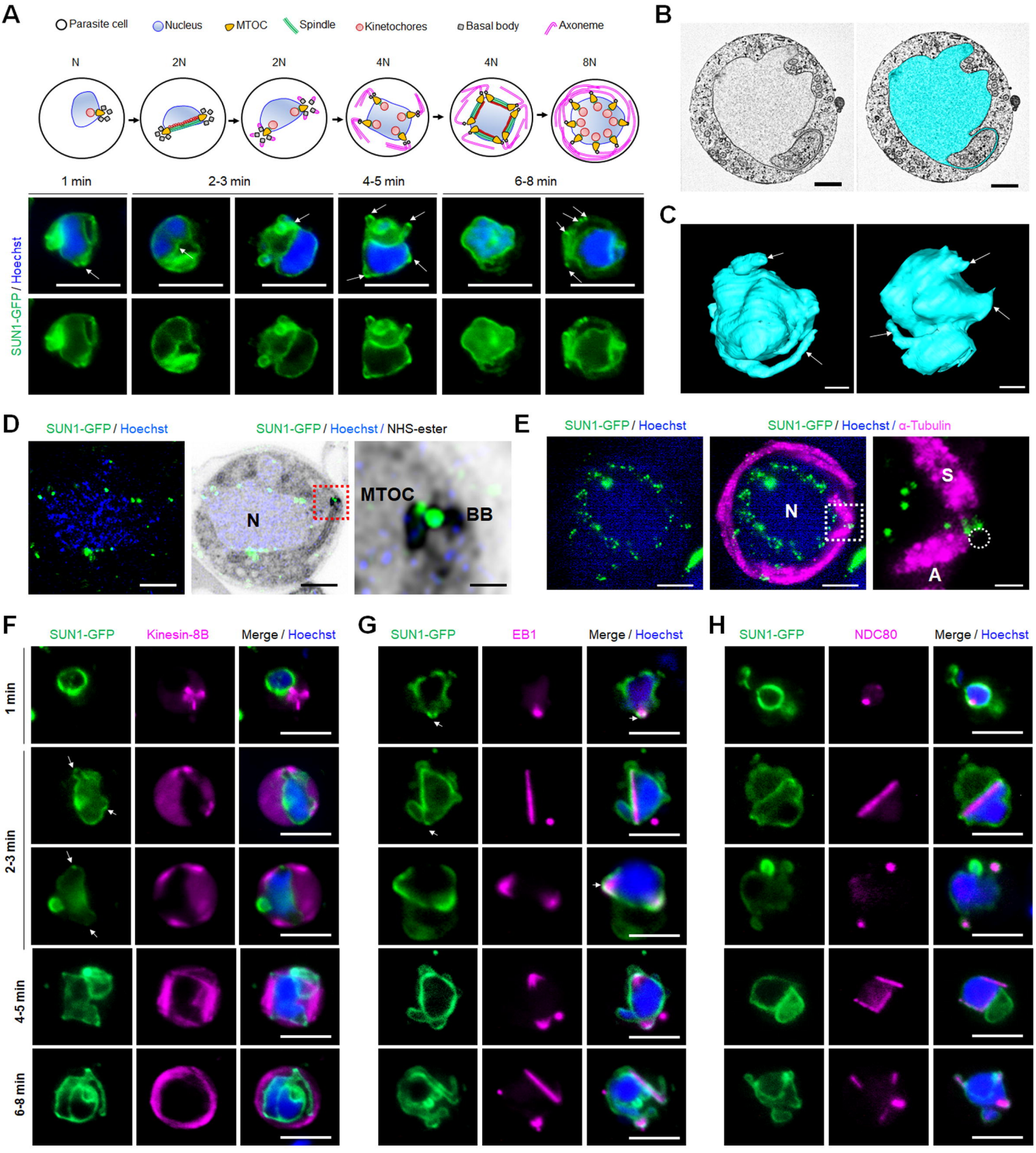
A
Parasite cell
Nucleus
MTOC
Spindle
Kinetochores
Basal body
Axoneme
N
2N
2N
4N
4N
8N
1 min
2-3 min
4-5 min
6-8 min
SUN1-GFP / Hoechst
B
C
D
SUN1-GFP / Hoechst
SUN1-GFP / Hoechst / NHS-ester
N
MTOC
BB
E
SUN1-GFP / Hoechst
SUN1-GFP / Hoechst / α-Tubulin
N
S
A
F
SUN1-GFP
Kinesin-8B
Merge / Hoechst
1 min
2-3 min
4-5 min
6-8 min
G
SUN1-GFP
EB1
Merge / Hoechst
H
SUN1-GFP
NDC80
Merge / Hoechst

Fig 2

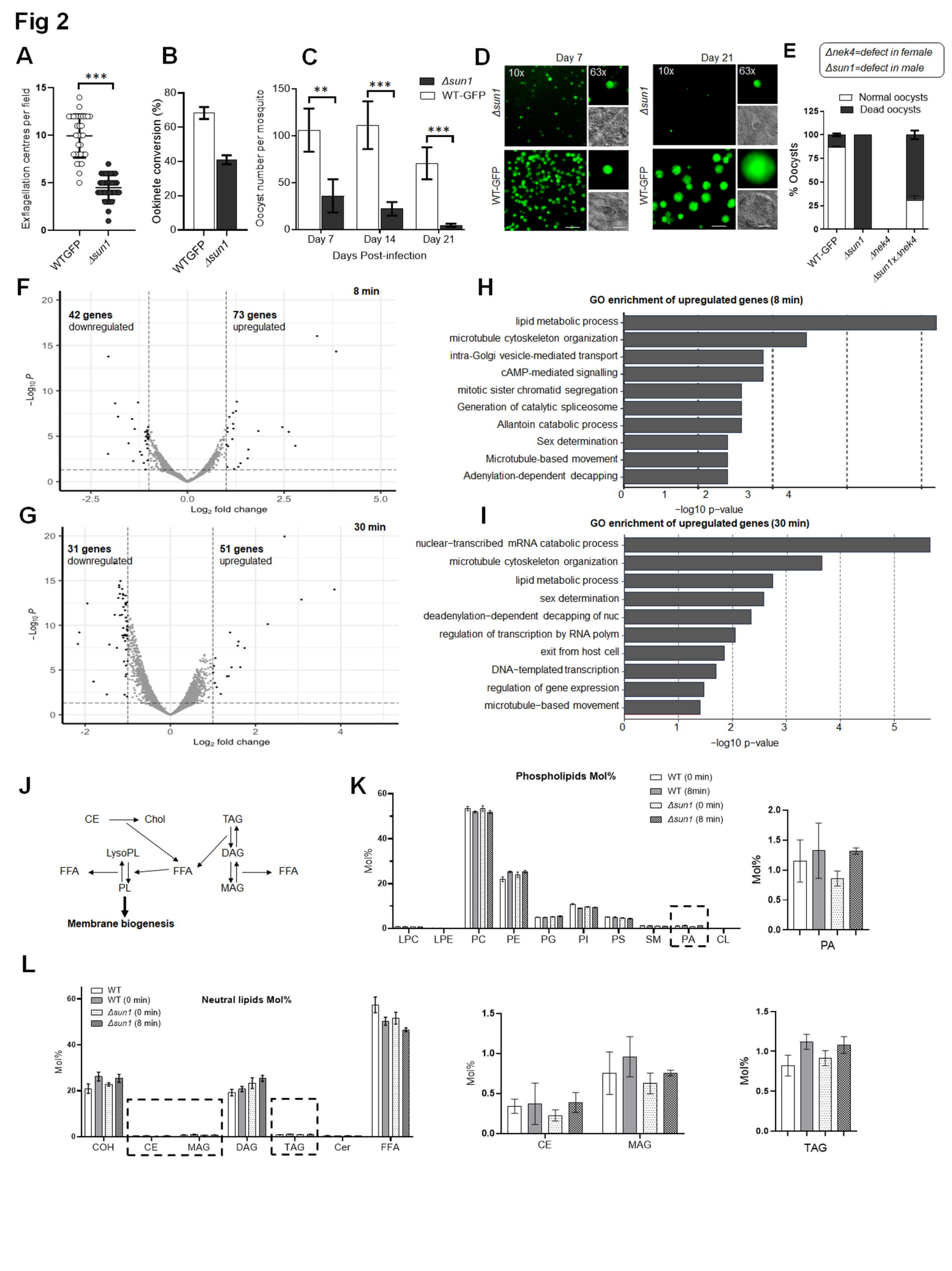
A
Exflagellation centres per field
***
WTGFP
Δsun1
B
Ookinete conversion (%)
WTGFP
Δsun1
C
Oocyst number per mosquito
**
***
***
Δsun1
WT-GFP
Day 7
Day 14
Day 21
Days Post-infection
D
Day 7
Day 21
10x
63x
Δsun1
WT-GFP
E
Δnek4=defect in female
Δsun1=defect in male
Normal oocysts
Dead oocysts
% Oocysts
WT-GFP
Δsun1
Δnek4
Δsun1xΔnek4
F
8 min
42 genes
downregulated
73 genes
upregulated
−Log10 P
Log2 fold change
G
30 min
31 genes
downregulated
51 genes
upregulated
−Log10 P
Log2 fold change
H
GO enrichment of upregulated genes (8 min)
lipid metabolic process
microtubule cytoskeleton organization
intra-Golgi vesicle-mediated transport
cAMP-mediated signalling
mitotic sister chromatid segregation
Generation of catalytic spliceosome
Allantoin catabolic process
Sex determination
Microtubule-based movement
Adenylation-dependent decapping
−log10 p−value
I
GO enrichment of upregulated genes (30 min)
nuclear−transcribed mRNA catabolic process
microtubule cytoskeleton organization
lipid metabolic process
sex determination
deadenylation−dependent decapping of nuc
regulation of transcription by RNA polym
exit from host cell
DNA−templated transcription
regulation of gene expression
microtubule−based movement
−log10 p−value
J
CE
Chol
TAG
LysoPL
DAG
FFA
FFA
FFA
PL
MAG
Membrane biogenesis
K
Phospholipids Mol%
WT (0 min)
WT (8min)
Δsun1 (0 min)
Δsun1 (8 min)
Mol%
LPC
LPE
PC
PE
PG
PI
PS
SM
PA
CL
PA
L
WT
WT (0 min)
Δsun1 (0 min)
Δsun1 (8 min)
Neutral lipids Mol%
Mol%
COH
CE
MAG
DAG
TAG
Cer
FFA
CE
MAG
TAG

Fig 3

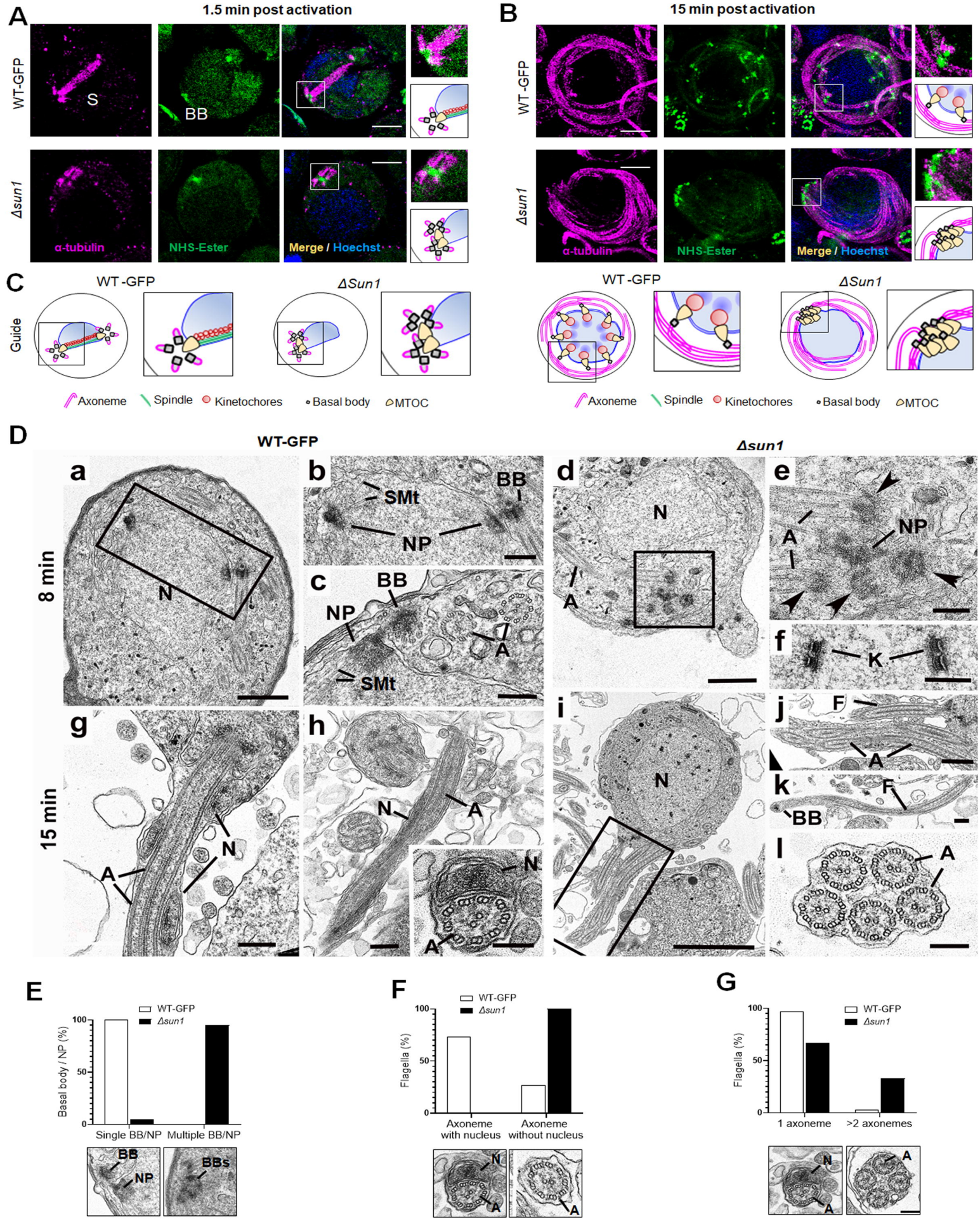
A
1.5 min post activation
WT-GFP
Δsun1
S
BB
α-tubulin
NHS-Ester
Merge / Hoechst
B
15 min post activation
C
Guide
WT-GFP
ΔSun1
Axoneme
Spindle
Kinetochores
Basal body
MTOC
D
WT-GFP
Δsun1
8 min
15 min
SMt
NP
N
A
K
F
E
Basal body / NP (%)
Single BB/NP
Multiple BB/NP
BBs
F
Flagella (%)
Axoneme with nucleus
Axoneme without nucleus
G
1 axoneme
>2 axonemes

A *WT-GFP vs. SUN1-GFP*

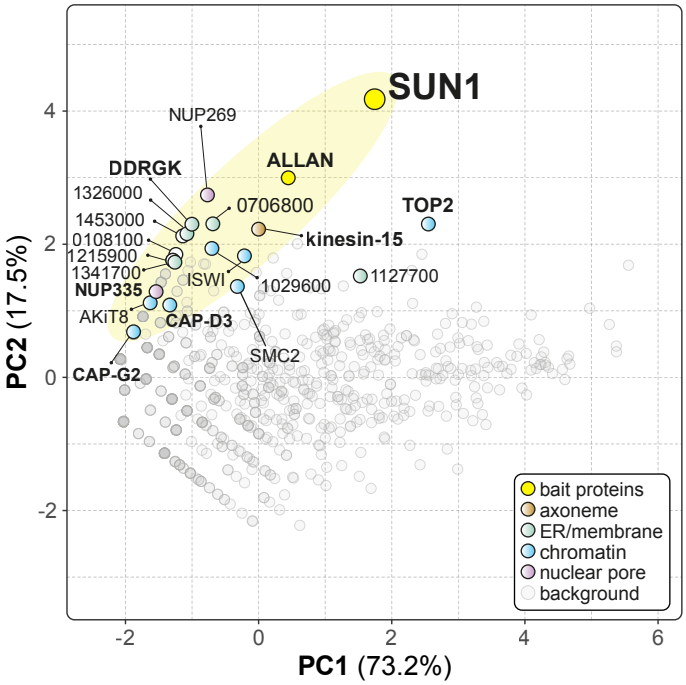

B *WT-GFP vs. ALLAN-GFP*

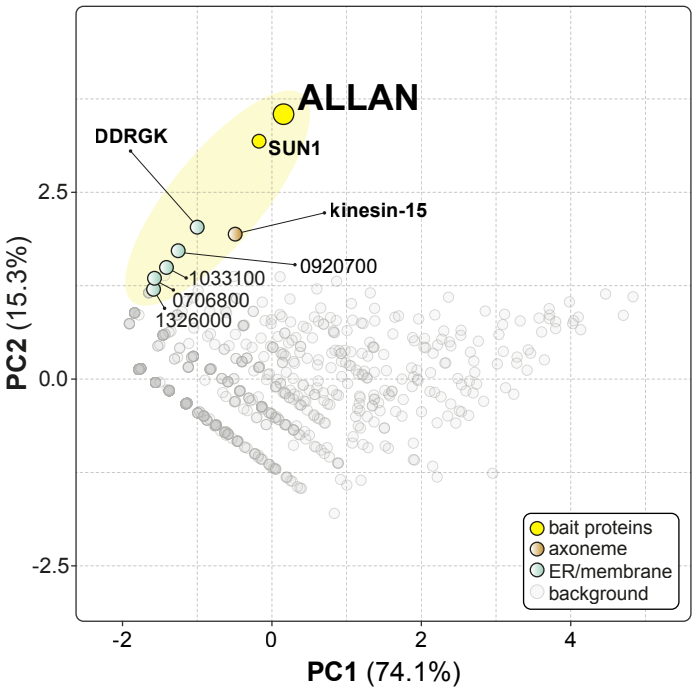

C

PBANKA	annotation	AA	GFP 1	GFP 2	SUN1 1	SUN1 2	ALLAN 1	ALLAN 2
1430900	**SUN domain-containing protein**	**872**	**-**	**-**	**47**	**49**	**29**	**2**
1304400	**allantoicase ALLAN**	**478**	**-**	**-**	**19**	**10**	**17**	**14**
1453000	conserved Plasmodium protein	1145	-	-	15	-	-	-
0108100	conserved Plasmodium protein	1109	-	-	10	-	-	-
1341700	ARM domain, unknown function	2004	-	-	9	-	-	-
1458800	**kinesin-15**	**1414**	**-**	**-**	**16**	**2**	**14**	**-**
1454600	NUP269	2260	-	-	28	-	-	-
0807900	NUP335	2840	-	-	5	-	-	-
0927700	**DDRGK domain - UFM1 E3 ligase**	**1889**	**-**	**-**	**17**	**-**	**5**	**1**
1127800	DnaJ protein (chaperone)	379	2	4	16	5	-	-
0706800	DnaJ protein (chaperone)	646	-	-	14	-	3	-
1326000	atlasin-like, GTP-binding protein	1297	-	-	15	-	2	-
1215900	dynamin-like	1262	-	-	9	-	-	-
0920700	fam-b protein	439	-	-	7	-	6	-
1011400	**DNA topoisomerase 2 (TOPO2)**	**1472**	**3**	**4**	**35**	**13**	**4**	**-**
0712100	DNA helicase ISWI	1018	-	-	10	2	-	-
1416900	SMC2 (condensin)	1227	-	-	7	2	-	-
1029600	Myb domain protein	376	-	-	8	2	-	-
0301800	condensin-2 complex subunit D3	1706	-	-	4	-	-	-
0213200	kinetochore protein AKiT8	2347	-	-	3	-	-	-
1312000	condensin-2 complex subunit G2	1181	-	-	3	-	-	-

Fig 5

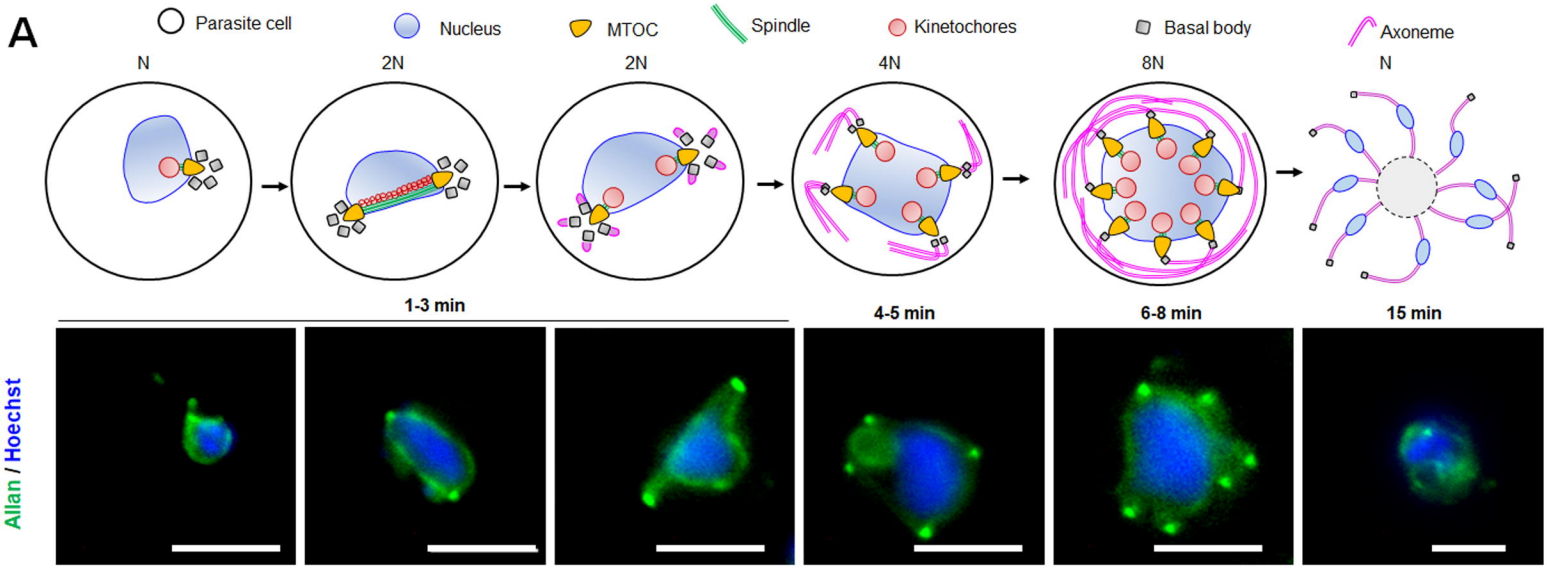
A
Parasite cell
Nucleus
MTOC
Spindle
Kinetochores
Basal body
Axoneme
N
2N
2N
4N
8N
N
1-3 min
4-5 min
6-8 min
15 min
Allan / Hoechst

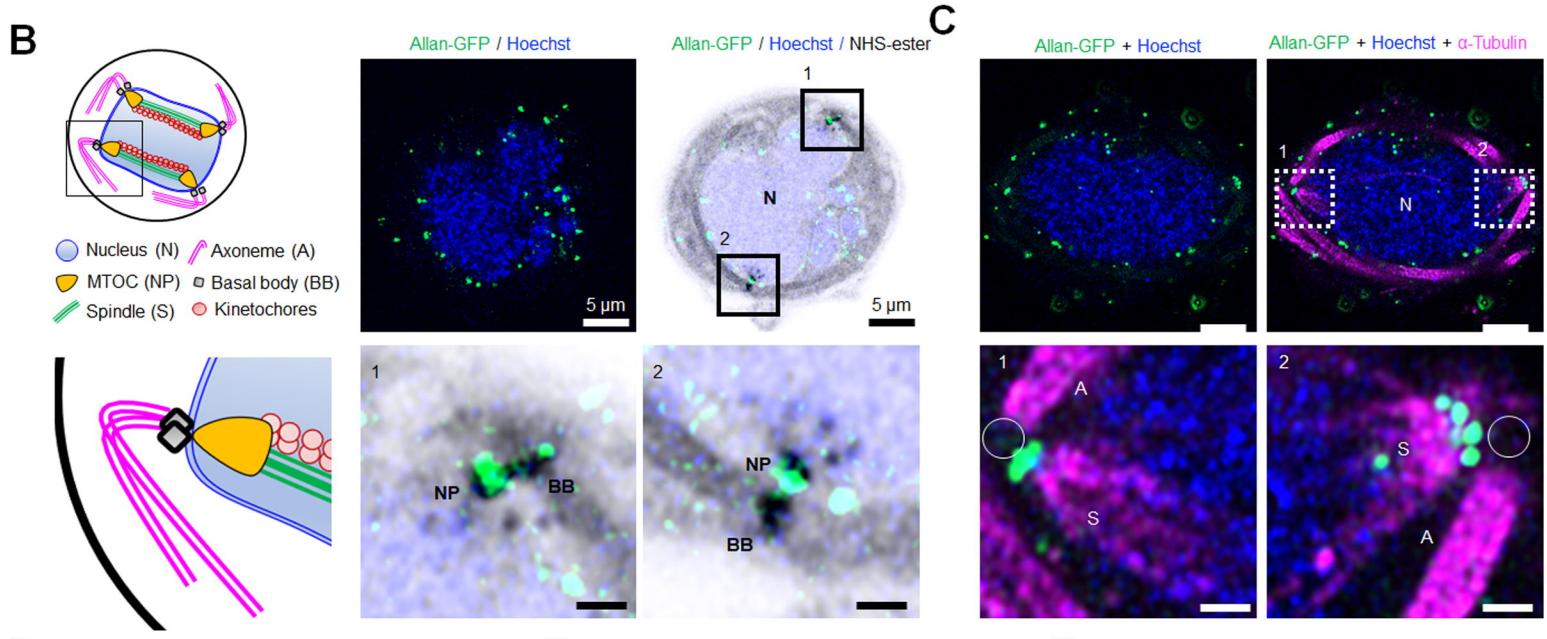
B
Nucleus (N)
Axoneme (A)
MTOC (NP)
Basal body (BB)
Spindle (S)
Kinetochores
Allan-GFP / Hoechst
5 µm
Allan-GFP / Hoechst / NHS-ester
N
5 µm
NP
BB
NP
BB
C
Allan-GFP + Hoechst
Allan-GFP + Hoechst + α-Tubulin
N
A
S
S
A

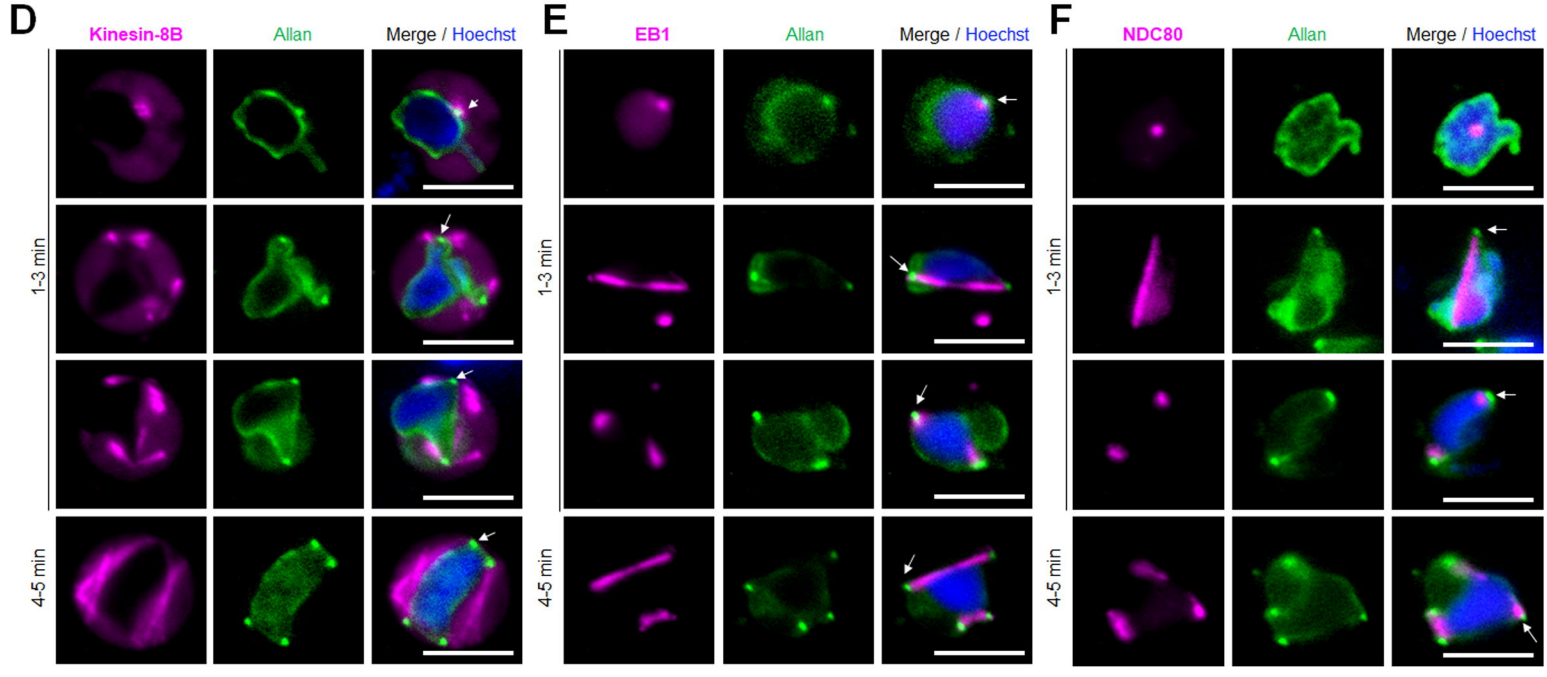
D
Kinesin-8B
Allan
Merge / Hoechst
1-3 min
4-5 min
E
EB1
Allan
Merge / Hoechst
1-3 min
4-5 min
F
NDC80
Allan
Merge / Hoechst
1-3 min
4-5 min

Fig 6

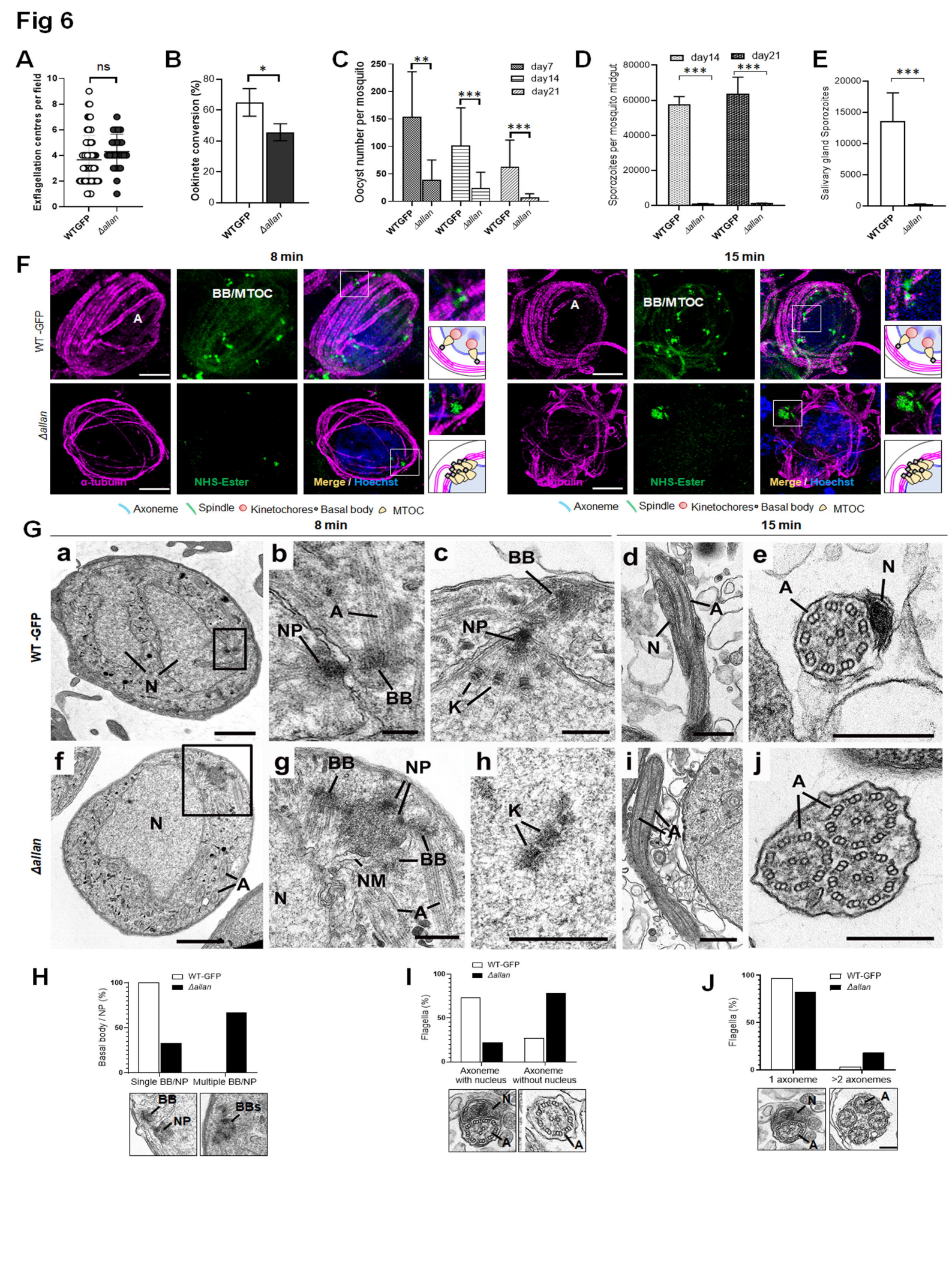
A
ns
Exflagellation centres per field
WTGFP
Δallan
B
*
Ookinete conversion (%)
C
**
***
***
Oocyst number per mosquito
day7
day14
day21
D
day14
day21
***
***
Sporozoites per mosquito midgut
E
***
Salivary gland Sporozoites
F
8 min
15 min
WT -GFP
Δallan
A
BB/MTOC
α-tubulin
NHS-Ester
Merge / Hoechst
Axoneme
Spindle
Kinetochores
Basal body
MTOC
G
8 min
15 min
WT -GFP
Δallan
a
b
c
d
e
f
g
h
i
j
N
A
NP
BB
K
NM
H
WT-GFP
Δallan
Basal body / NP (%)
Single BB/NP
Multiple BB/NP
BBs
I
Flagella (%)
Axoneme with nucleus
Axoneme without nucleus
J
1 axoneme
>2 axonemes

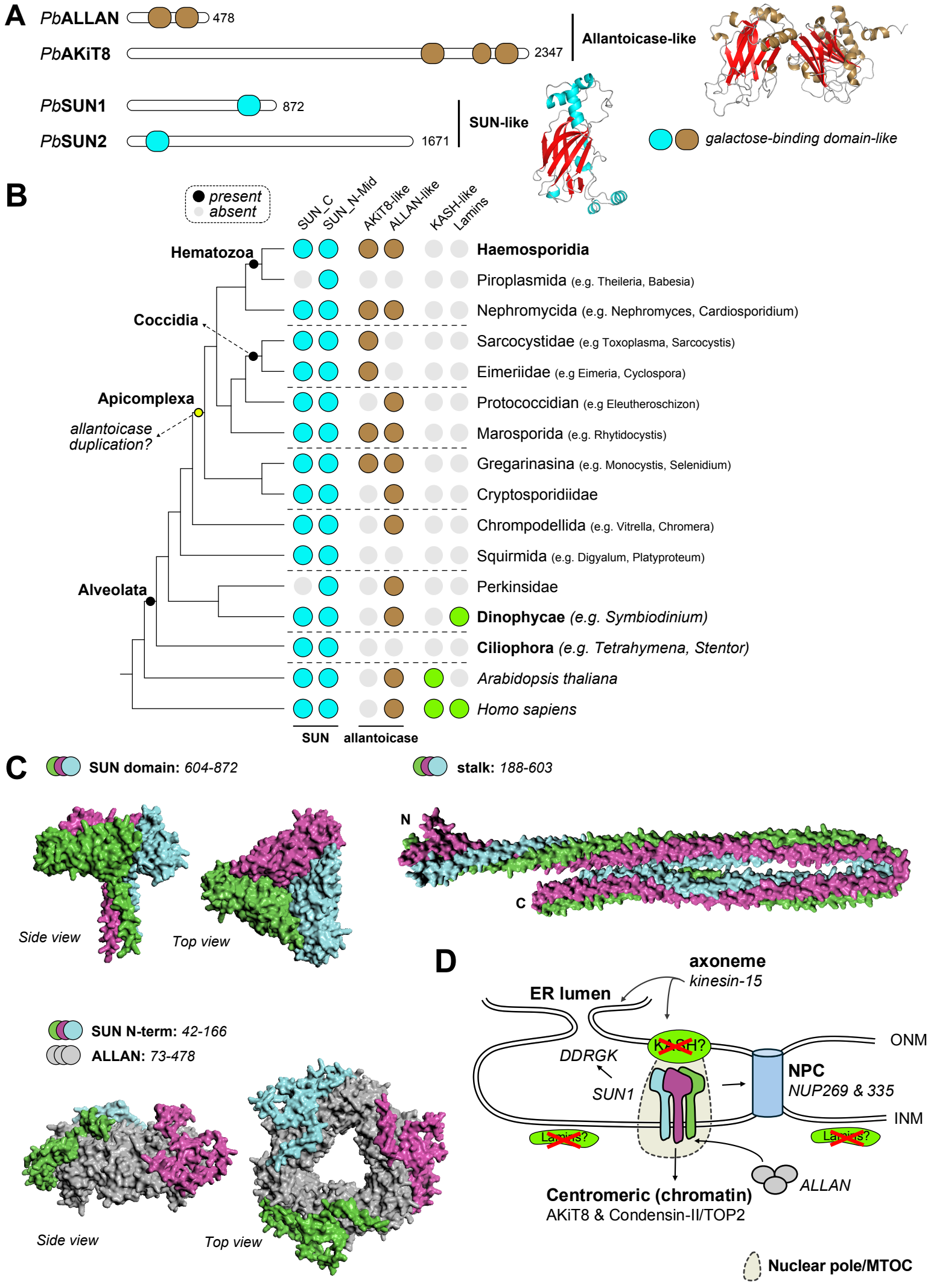
A
PbALLAN
478
PbAKiT8
2347
Allantoicase-like
PbSUN1
872
PbSUN2
1671
SUN-like
galactose-binding domain-like
B
present
absent
SUN_C
SUN_N-Mid
AKiT8-like
ALLAN-like
KASH-like
Lamins
Hematozoa
Haemosporidia
Piroplasmida (e.g. Theileria, Babesia)
Nephromycida (e.g. Nephromyces, Cardiosporidium)
Coccidia
Sarcocystidae (e.g Toxoplasma, Sarcocystis)
Eimeriidae (e.g Eimeria, Cyclospora)
Apicomplexa
Protococcidian (e.g Eleutheroschizon)
allantoicase duplication?
Marosporida (e.g. Rhytidocystis)
Gregarinasina (e.g. Monocystis, Selenidium)
Cryptosporidiidae
Chrompodellida (e.g. Vitrella, Chromera)
Squirmida (e.g. Digyalum, Platyproteum)
Alveolata
Perkinsidae
Dinophycae (e.g. Symbiodinium)
Ciliophora (e.g. Tetrahymena, Stentor)
Arabidopsis thaliana
Homo sapiens
SUN
allantoicase
C
SUN domain: 604-872
stalk: 188-603
Side view
Top view
N
C
SUN N-term: 42-166
ALLAN: 73-478
Side view
Top view
D
axoneme
kinesin-15
ER lumen
KASH?
DDRGK
SUN1
ONM
NPC
NUP269 & 335
INM
Lamins?
Lamins?
ALLAN
Centromeric (chromatin)
AKiT8 & Condensin-II/TOP2
Nuclear pole/MTOC